



Developmental origins of mosaic evolution in the avian cranium

Ryan N. Felice^{a,b,1} and Anjali Goswami^{a,b,c}

^aDepartment of Genetics, Evolution, and Environment, University College London, London WC1E 6BT, United Kingdom; ^bDepartment of Life Sciences, The Natural History Museum, London SW7 5DB, United Kingdom; and ^cDepartment of Earth Sciences, University College London, London WC1E 6BT, United Kingdom

Edited by Neil H. Shubin, The University of Chicago, Chicago, IL, and approved December 1, 2017 (received for review September 18, 2017)

Mosaic evolution, which results from multiple influences shaping morphological traits and can lead to the presence of a mixture of ancestral and derived characteristics, has been frequently invoked in describing evolutionary patterns in birds. Mosaicism implies the hierarchical organization of organismal traits into semiautonomous subsets, or modules, which reflect differential genetic and developmental origins. Here, we analyze mosaic evolution in the avian skull using high-dimensional 3D surface morphometric data across a broad phylogenetic sample encompassing nearly all extant families. We find that the avian cranium is highly modular, consisting of seven independently evolving anatomical regions. The face and cranial vault evolve faster than other regions, showing several bursts of rapid evolution. Other modules evolve more slowly following an early burst. Both the evolutionary rate and disparity of skull modules are associated with their developmental origin, with regions derived from the anterior mandibular-stream cranial neural crest or from multiple embryonic cell populations evolving most quickly and into a greater variety of forms. Strong integration of traits is also associated with low evolutionary rate and low disparity. Individual clades are characterized by disparate evolutionary rates among cranial regions. For example, Psittaciformes (parrots) exhibit high evolutionary rates throughout the skull, but their close relatives, Falconiformes, exhibit rapid evolution in only the rostrum. Our dense sampling of cranial shape variation demonstrates that the bird skull has evolved in a mosaic fashion reflecting the developmental origins of cranial regions, with a semi-independent tempo and mode of evolution across phenotypic modules facilitating this hyperdiverse evolutionary radiation.

evolutionary rates | evolutionary development | modularity | morphological diversity | morphometrics

The term “mosaic evolution” was coined following the discovery of body fossils of *Archaeopteryx*, the iconic early bird, which fascinated researchers with its combination of ancestral “reptilian” and derived avian features (1, 2). Mosaic evolution has since become a central part of understanding avian origins and diversification (3–6), but it is rarely quantified (7). Mosaic evolution is the result of traits evolving at different rates or with different modes. For example, the diversification of locomotor behaviors in birds is thought to be related to the evolutionary independence of the forelimb and hind limb (3, 4, 8). Strongly correlated traits are expected to have a coordinated response to selection, whereas dissociated traits can evolve independently. These relationships among traits are governed by genetic, developmental, and functional associations that can form semiautonomous modules.

The tetrapod skull exhibits developmental modularity: the face is primarily derived from cranial neural crest (CNC) cells, whereas the braincase has a primarily mesodermal origin. This dichotomy is the basis of many investigations of phenotypic modularity in the skull: skeletal elements sharing a common embryonic origin can be predicted to covary with each other more than with components of different origins (9, 10). Finer-scale studies of craniofacial development have uncovered examples of phenotypic modularity in the skull regulated by the expression of a small number of

genes. For example, manipulating the expression of *Fgf8* generates correlated responses in the growth of the premaxilla and palatine in archosaurs (11). Similarly, variation in avian beak shape and size is regulated by two separate developmental modules (7). Despite the evidence for developmental modularity in the avian skull, some studies have concluded that the cranium is highly integrated (i.e., not subdivided into semiautonomous modules) (9, 10, 12). In light of recent evidence that diversity in beak morphology may not be shaped by dietary factors (12), it is especially critical to investigate other factors that shape the evolution of cranial variation, such as developmental interactions/constraint. Here, we evaluate hypotheses of cranial modularity using a high-dimensional geometric morphometric dataset of unprecedented resolution (757 3D landmarks) that comprehensively describes cranial shape and broad sampling across Neornithes (352 species).

A key question in the study of phenotypic modularity is how trait interactions influence macroevolutionary change (13–15). For example, high integration is frequently hypothesized to constrain disparity and evolutionary rate by limiting axes of variation upon which selection can act and thus limiting the direction or magnitude of response to selection (13, 14). This has been supported with empirical data from cranial modules in primates and carnivores in which there is an overall positive relationship between integration and constraint (14). In contrast, in the felid axial skeleton high integration has the opposite effect,

Significance

Studies reconstructing morphological evolution have long relied on simple representations of organismal form or on limited sampling of species, hindering a comprehensive understanding of the factors shaping biological diversity. Here, we combine high-resolution 3D quantification of skull shape with dense taxonomic sampling across a major vertebrate clade, birds, to demonstrate that the avian skull is formed of multiple semi-independent regions that epitomize mosaic evolution, with cranial regions and major lineages evolving with distinct rates and modes. We further show that the evolvability of different cranial regions reflects their disparate embryonic origins. Finally, we present a hypothetical reconstruction of the ancestral bird skull using this high-resolution shape data to generate a detailed estimate of extinct forms in the absence of well-preserved three-dimensional fossils.

Author contributions: R.N.F. and A.G. designed research, performed research, analyzed data, and wrote the paper.

The authors declare no conflict of interest.

This article is a PNAS Direct Submission.

This open access article is distributed under Creative Commons Attribution-NonCommercial-NoDerivatives License 4.0 (CC BY-NC-ND).

Data deposition: Scan data used in this study will be available for download from [Phenome10K.org](#), subject to copyright rules of the respective repositories.

¹To whom correspondence should be addressed. Email: ryanfelice@gmail.com.

This article contains supporting information online at [www.pnas.org/lookup/suppl/doi:10.1073/pnas.1716437115/-DCSupplemental](#).

promoting greater response to selection (16). Analysis of simulated data has suggested that integration does not necessarily influence evolutionary rate or disparity but rather the direction of response to selection (13). We reconstruct macroevolutionary dynamics across modules in the present dataset to further disentangle the complicated relationships between integration, development, and diversification.

Results

Using a likelihood-based approach for comparing hypotheses of modularity (17) and covariance ratio analysis (18), we find support for the avian skull as highly modular and consisting of seven anatomical modules (Fig. 1 A and B), similar to patterns of organization observed in mammals (17, 19). This contrasts with previous analyses that have found the avian cranium to be highly integrated. However, these previous analyses have been restricted to analyzing smaller clades (10, 12) or have excluded large portions of the skull (9).

We computed the rate of evolution in each module directly from the landmark configurations (20) using a recently published dated phylogeny for birds (21). The rostrum, palate, naris, and cranial vault evolve at the fastest rates ($\sigma^2_{\text{mult}} = 2.98 \times 10^{-7}$ – 3.82×10^{-7} , SI Appendix, Table S1). The occipital and pterygoid-quadrilateral evolve approximately one-third as fast ($\sigma^2_{\text{mult}} = 1.15 \times 10^{-7}$ – 1.23×10^{-7}), and the basisphenoid exhibits the lowest rate ($\sigma^2_{\text{mult}} = 0.72 \times 10^{-7}$). Overall, there is an inverse relationship between rate and within-module integration (Fig. 2A). Similarly, we observe an inverse relationship between disparity (Procrustes variance) and integration (Fig. 2B). These patterns are associated with differences in developmental complexity: the fast-evolving modules develop from anterior mandibular-stream CNC cells only (nares) or with contributions from multiple embryonic cell types including the anterior mandibular-stream CNC cells (rostrum, palate, vault), whereas the more slowly evolving regions arise from either the posterior mandibular CNC only (pterygoid-quadrilateral) or mesoderm only (occipital and basisphenoid) (22). Together, these findings suggest that strong within-module trait correlations, related to developmental origin, constrain both the rate of evolution and the potential for the evolution of high diversity in some avian cranial modules, as in mammals (23).

For each anatomical module, we conducted evolutionary model fitting on the principal component axes that explain 95% of the within-module variation (SI Appendix, Table S1) to detect shifts in evolutionary rates across the Neornithes. Brownian motion with a lambda tree transformation is the most likely model for the whole skull and for each individual module. High lambda values (mean $\lambda = 0.83$ – 0.94) emphasize that phenotype is strongly influenced by shared ancestry. Multivariate phylogenetic signal (24) is lower for each module ($K_{\text{mult}} = 0.48$ – 0.66 , $P = 0.001$, SI Appendix, Table S1) but still indicates a significant effect of phylogeny on morphology. Tracing evolutionary rate through time illustrates that each module experienced high rates early in the diversification of birds, leading up to and corresponding with the Cretaceous–Paleogene (K–Pg) boundary (Fig. 1C). This pattern is concordant with recent reconstructions of high net species diversification rates in the latest Cretaceous (25) and with the estimated time of the origination of major clades including Neoaves, Strisores, Inopaves, Aequorlitorinthes, and Columbaves (21). This peak is likely to be a result of the origin of major phenotypic innovations early in the diversification of these clades. Phenotypic evolutionary rates are very low immediately following the K–Pg mass extinction. Perhaps representing a signal of recovery from the extinction event, there is a small peak centered around 60 Mya, coinciding with the origin of several orders including Sphenisciformes, Coliiformes, Musophagiformes, and Accipitriformes (21). Fossil evidence indicates that these clades had begun to acquire key phenotypic differences during this interval (26, 27). In the rostrum, vault, and pterygoid-quadrilateral, rates

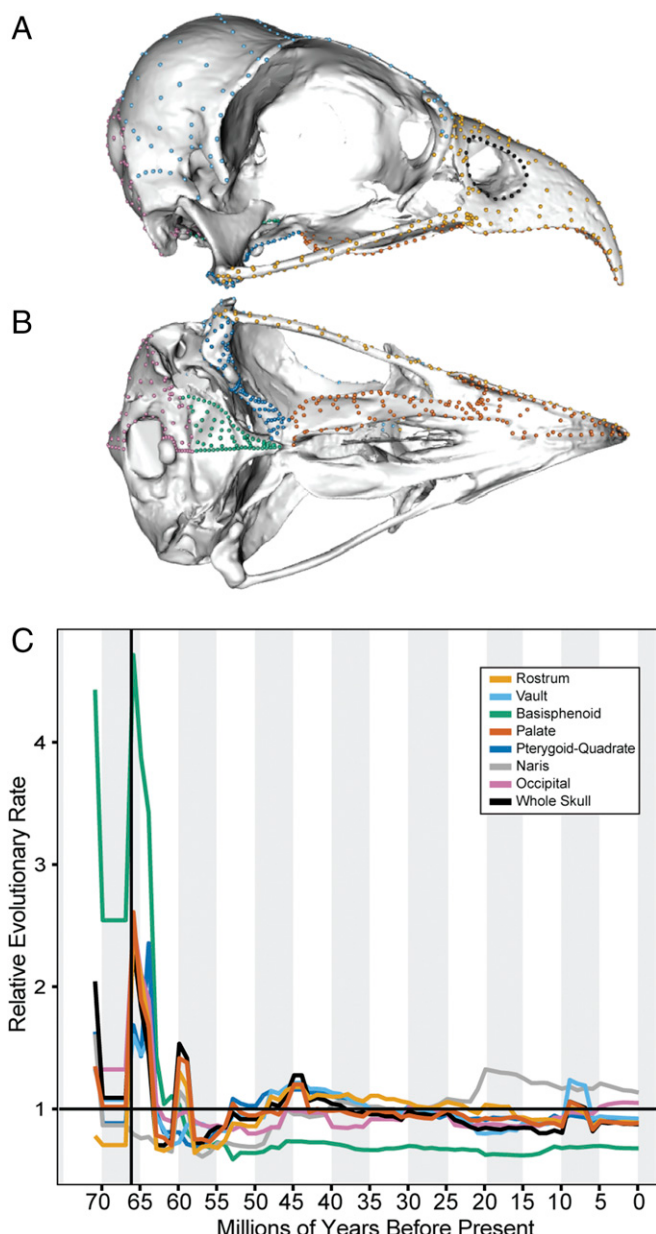


Fig. 1. Cranial modularity in the avian skull. Cranial morphology was quantified using 757 3D landmarks, here illustrated on *Pandion haliaetus* (USNM 623422) in lateral (A) and ventral (B) perspective. Landmark colors reflect the reconstructed pattern of seven cranial modules. (C) Rate through time plots for each of the seven modules and the whole skull.

accelerate gradually through the Eocene, peaking at 45 Mya. This was a major period of cladogenesis: Charadriiformes, Anseriformes, Galliformes, and Strigiformes all originated in this interval. Finally, the rostrum, vault, and palate modules exhibit a peak in rates between 5 and 10 Mya. This is likely to represent recent intrafamilial and intrageneric divergences.

We further examined the patterns of rate shifts throughout the tree to understand the tempo and mode of evolution in each module across different lineages. For each module, rapid evolutionary change tends to occur (i) at the origin of major clades, (ii) throughout the evolution of diverse clades, and/or (iii) in association with the acquisition of novel phenotypes relative to the broader sample. These patterns are typified by the rostrum module. Falconiformes, Anatidae, Strisores, and Pelecaniformes

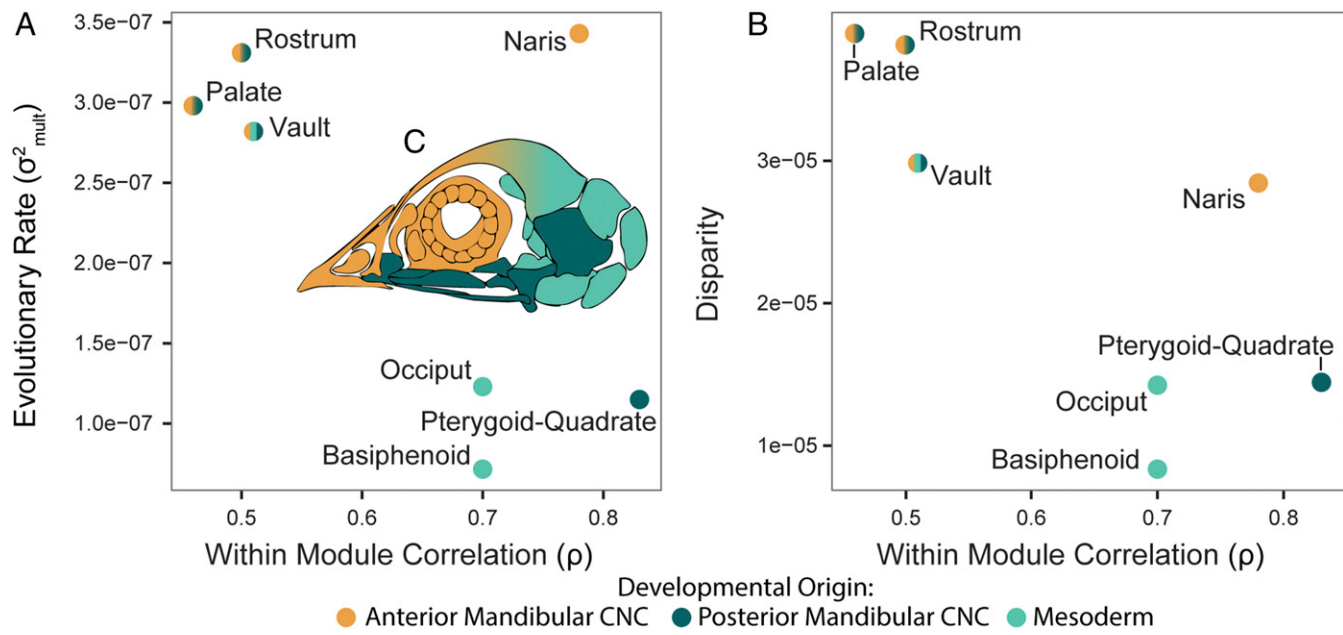


Fig. 2. Module integration and evolution reflects developmental origin. Evolutionary rate vs. within-module correlation (A) and disparity vs. within-module correlation (B). Disparity is quantified for each module using Procrustes variance divided by the number of landmarks. Disparity and rate are highest in modules that are composed of anterior mandibular CNC or multiple embryonic cell types. Embryonic origin of cranial elements is shown in C, modified from ref. 22.

exhibit bursts of rapid rostrum evolution at their origins (Fig. 3 and *SI Appendix*, Fig. S1). Core Passeroidea (28) exhibits an early burst with sustained elevated rates relative to other passeriforms. Within Coraciimorphae, the highest estimated rates of rostrum evolution are exhibited by hornbills (Bucerotidae) and toucans (Ramphastidae), which are frequently cited as classic examples of Old World and New World phenotypic convergence for their long, broad bills (29). Lineages with unique beak phenotypes (relative to their parent clade in the present sample) and rapid rostrum evolution include Pelecanidae, Recurvirostridae, Phoenicopteridae, *Campylorhamphus*, *Psarocolius*, *Rostratula*, and *Nyctibius* (*SI Appendix*, Fig. S1). Overall patterns of rostrum-shape evolution are comparable to those reconstructed in a recent study of bill evolution (30). As in the rostrum, the bill is characterized by bursts of “quantum evolution” at the origin of major clades, as well as by rapid evolution on branches leading to the first occurrence of a unique phenotype within the given sample (30).

This pattern of early bursts and quantum evolution alongside acceleration in some unusual lineages is also observed in other modules. Psittaciformes, Bucerotiformes, and Passeroidea show very similar patterns in the palate and rostrum (Fig. 4A and *SI Appendix*, Fig. S2). The high ancestral rate at the origin of Psittaciformes is presumably associated with the evolution of the characteristic vertically oriented palatine (31). Rates of evolution in the cranial vault are less variable, with bursts of rapid evolution at the origin of Strigiformes, Strisores, and Trochilidae (Fig. 4B). The highest rates of cranial vault evolution are seen in genera with cranial ornaments (e.g., *Casuarius*, *Numida*, *Balearica*, *Bucorvus*), suggesting that display structures may evolve particularly quickly (*SI Appendix*, Fig. S3) (32).

Each of the other cranial modules also exhibit distinct and heterogeneous patterns of evolutionary rate (*SI Appendix*, Figs. S4–S8). The occipital region is characterized by sustained evolutionary rates throughout major clades, including high rates in Passeri and Phasianidae (Fig. 4C). The most notable rate shift in the pterygoid-quadrata module includes early bursts at the origin of Strisores, Gallonserae, and the most recent common ancestor of Strigiformes and Piciformes and sustained high rates in Psittaciformes (*SI Appendix*, Fig. S5). In the naris module, patterns

are largely defined by clades with divergent naris morphology or position such as Bucerotidae and Ramphastidae, which both have extremely posteriorly positioned nares (*SI Appendix*, Fig. S6). Finally, the basisphenoid module has the slowest overall rate of evolution observed across the skull, but quantum evolution is observed at the origin of several groups including Strisores, Aequorlitornithes, and Trochilidae (*SI Appendix*, Fig. S7). This module most typifies an early burst, with the highest rates in the Late Cretaceous and lowest rates in the Cenozoic (Fig. 1C).

The earliest crown bird fossils include representatives of Galloanserae (33), total-clade Sphenisciformes (26), and total-clade Coliiformes (27). However, these specimens are known from primarily postcranial remains or highly deformed specimens, hindering estimation of the cranial phenotype for the ancestral neornithine. An advantage of high-dimensional geometric morphometrics is that it allows for the visualization of hypothetical phenotypes (34). We reconstructed the ancestral state for each module to generate a composite hypothesis of the earliest neornithine using a likelihood-based approach (35). Ancestral values were calculated from the Procrustes-aligned right-hand landmarks. This ancestral landmark configuration was projected into principal component morphospace along with the empirically derived specimens to find the species that it most closely resembles: *Vanga curvirostris*. The 3D mesh of *V. curvirostris* (*SI Appendix*, Fig. S9) was warped (36) to match the ancestral character state, generating the reconstruction shown in Fig. 3 (Inset). The reconstructed skull (Fig. 3) has a gently curved beak that is approximately equal in length to the rest of the skull and elongate choanae [schizognathous palate (31)]. In addition to *V. curvirostris*, overall skull shape is similar to that of *Oriolus oriolus*. Both are omnivorous passeriforms that are aerial and canopy foragers and range in mass from 64 to 79 g (37). This reconstruction serves as a first attempt at visualizing a hypothesis of avian origins using high-dimensional data and as a testable model of ancestral phenotype and potential feeding ecology. The accuracy of this reconstruction will be greatly improved by incorporation of data from extinct species (38), whether through discoveries of fossils that are well preserved in 3D or retrodeformation of existing fossils of both early crown and stem birds.

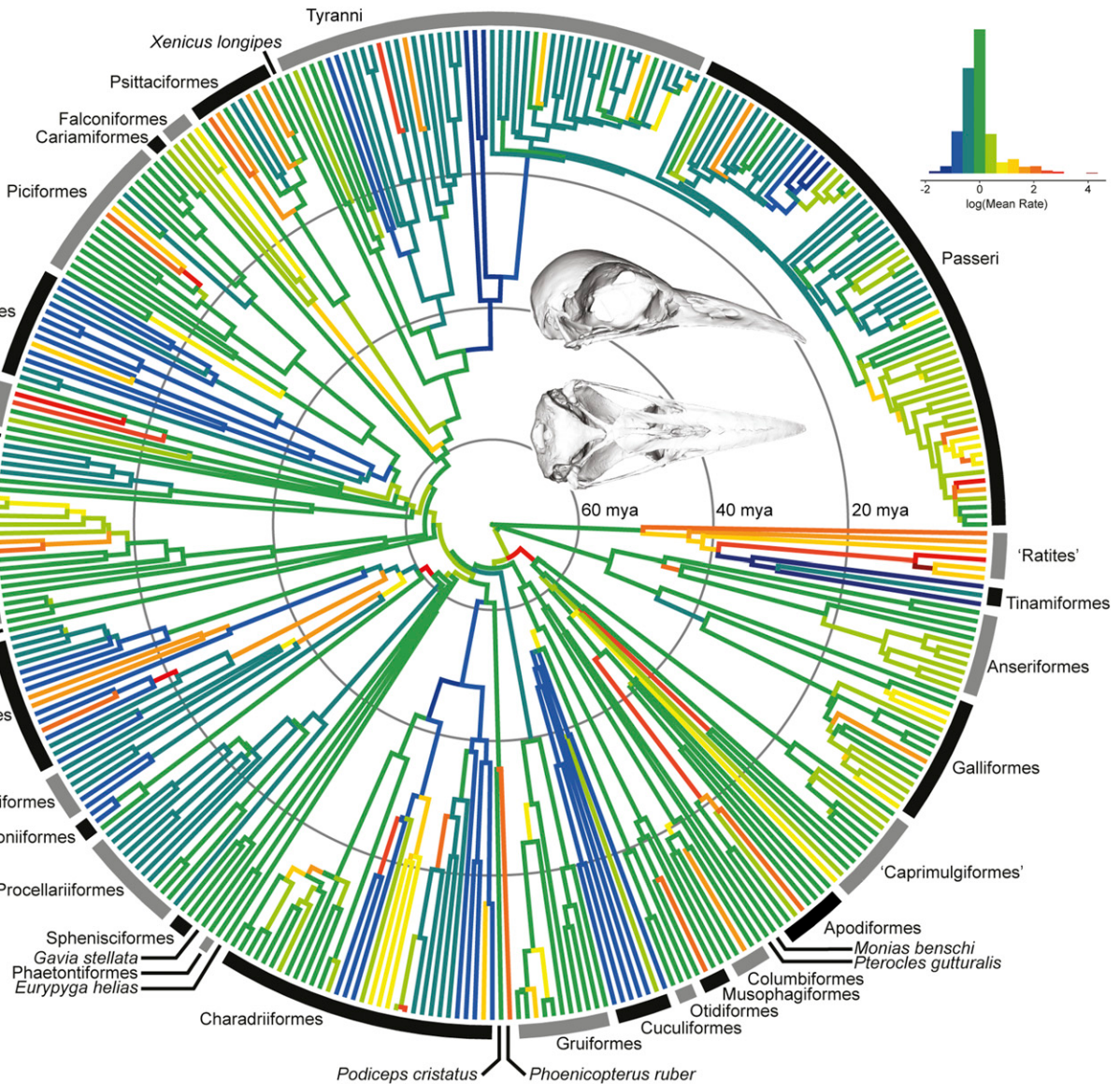


Fig. 3. Evolutionary rates in the avian rostrum. Estimated using BayesTraitsV3 using a variable-rates model and lambda tree transformation. (Inset) Reconstruction of the ancestral neornithine skull (*Materials and Methods*).

Discussion

Using high-dimensional morphometrics, we find that the avian skull is more modular than previously known (9, 10, 12). Weak correlations among anatomical modules allowed each to evolve relatively independently of the others, generating a pattern of mosaicism that characterizes several aspects of avian evolution (3–6). For each module, evolutionary rates vary greatly across clades. Morphologically diverse clades, including Strisores, Aequorlornithes (waterbirds and shorebirds), and Passeroidea, have elevated evolutionary rates at their origin in multiple modules. In contrast, Columbaves and Coraciiformes tend to evolve slowly in all modules. As in the avian bill, high rates of evolution are associated with the origin of divergent or unique phenotypes among the sampled taxa (30) including elongate or curved premaxillae (e.g., Phoenicopteridae), cranial ornaments (e.g., *Bucorvus*), or distinctive palates (e.g., Psittaciformes).

The finding that high integration is associated with low evolutionary rates and low disparity supports the long-standing hypothesis that strong correlations among traits constrain evolutionary

change. A similar pattern has been demonstrated in the mammal cranium (14). However, this pattern may not represent a general property of phenotypic integration as the strength of within-module correlation is positively correlated with disparity in other systems (16). Rather, the macroevolutionary consequences of integration are likely to be highly dependent on the direction and magnitude of selection on each module (13). Complementary analyses of other clades and anatomical regions will aid in expanding our understanding of the link between integration and constraint. Interestingly, we find a major difference in developmental complexity between modules with high and low integration: weakly integrated modules arise from multiple embryonic cell populations whereas strongly integrated modules are composed of just one. This mirrors the finding that, in mammals, anatomical modules with high developmental complexity have low within-module integration (23). Additional study of the functional and developmental constraints on cranial evolution, incorporating data from the brain and soft tissues, will allow for further evaluation of the mechanistic underpinnings of these patterns. For example, the morphogenetic primacy of the brain in

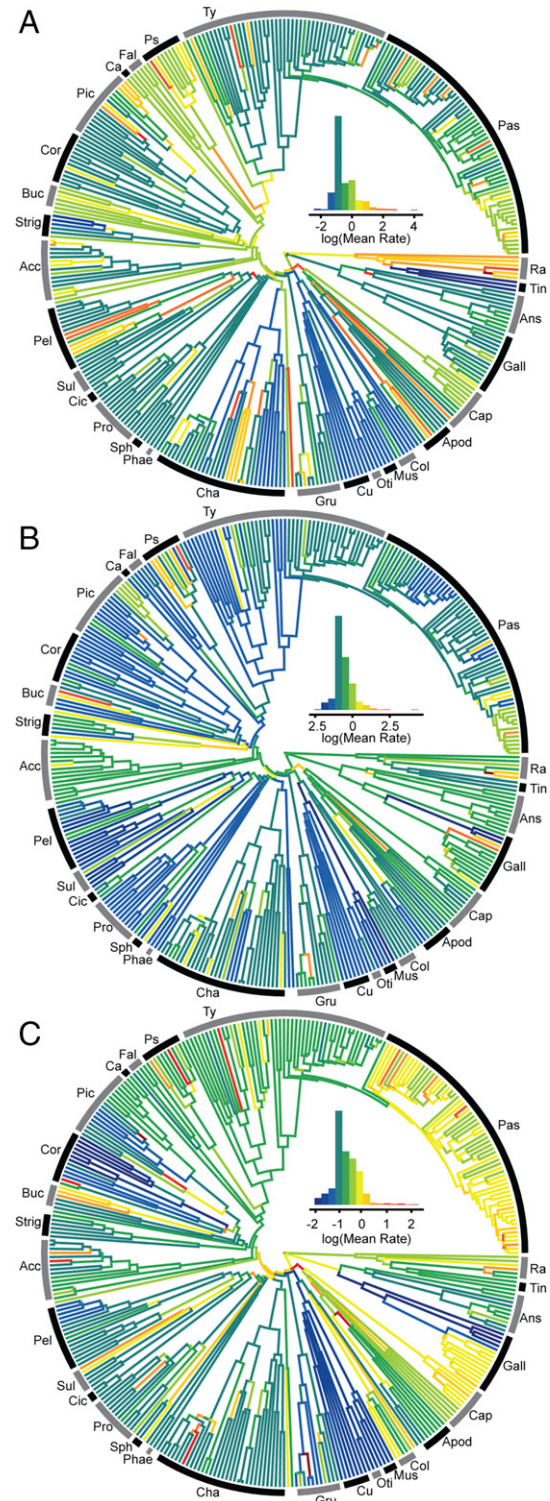


Fig. 4. Evolutionary rates across cranial modules. Palate (A), cranial vault (B), and occiput (C). Clade abbreviations: Acc, Accipitridae; Ans, Anseriformes; Apod, Apodidae; Buc, Bucerotidae; Cap, Caprimulgidae; Cor, Coraciidae; Gall, Galloanseriformes; Grui, Gruidae; Mus, Musophagidae; Oti, Otididae; Pas, Passeridae; Pel, Pelecanidae; Ps, Psittacidae; Ra, Ratites; Sph, Spheniscidae; Strig, Strigidae; Sul, Sulidae; Tin, Tinamidae; Ty, Tyrannidae.

the development of the cranium (39) may contribute to the relatively limited variation in evolutionary rates observed in the vault in this study. Taken together, these results support the fundamental prediction that macroevolutionary patterns are shaped by phenotypic modularity and integration, which are in turn determined by developmental processes (7, 11, 13, 16, 23).

From *Archaeopteryx* to crown birds, mosaic evolution has been a vital part of avian diversification. Mosaic evolution is possible because the cranium, like the brain (6) and postcranium (2–4), is composed of modular subunits that evolve at different rates in different lineages. Our high-density sampling of morphology and phylogeny allowed for identification of complex patterns of evolution that gave rise to the extraordinary diversity of living birds. Our results show that individual regions of the skull experienced independent rapid bursts of evolution at different times during the early adaptive radiation of Neornithes and later at the origin of some clades. We further demonstrate that structures derived from multiple embryonic cell types or from anterior mandibular CNC evolve at faster rates than those originating from only posterior mandibular CNC or mesoderm, highlighting the importance of intrinsic factors in shaping the evolution of biodiversity.

Materials and Methods

Data Collection. Skull morphology was characterized in 352 species of neognathine birds representing 320 genera and 159 families of the 238 families recognized by the International Ornithological Congress (*SI Appendix, Data File S1*). One specimen was digitized per species using laser surface scanning (FARO EDGE Scan Arm HD) or microCT scanning (SkyScan1172). For sexually dimorphic taxa, the sex with smaller or absent ornaments was selected for scanning. Because this study concerns skeletal evolution, crania were scanned without the rhamphotheca. Digital models were landmarked with 36 anatomical landmarks (26 bilateral, 10 midline) and 23 sliding semilandmark curves composed of a total of 335 landmarks (*SI Appendix, Data File S2*). Landmark placement was carried out using IDAV Landmark (34), and landmarking was conducted by a single investigator to avoid multiuser bias in placement.

Because some museum specimens are partially damaged or incomplete, semilandmark curves were digitized on the right side of the specimen and midline only. To generate an extremely detailed characterization of the entire surface of the skull, we then used a semiautomated procedure to distribute surface sliding semilandmarks across the skull. First, landmarks and semilandmark curves were placed on a simple hemispherical template (*SI Appendix, Fig. S10B*). Surface semilandmark points were placed on this template on the surface of the regions corresponding to the rostrum, jugal bar, cranial vault, occipital bones, basiphenoid, palate, and the ventral surfaces of the quadrate and pterygoid. We then used the R package Morpho (40) to apply the surface semilandmarks from the template to each specimen, generating a dataset of 770 landmarks per specimen (*SI Appendix, Fig. S10C*). Because the structure of the face, anterior orbit, and nares of ratites is substantially different from other birds, a separate rostrum template was used to ensure proper placement of the rostrum-surface semilandmarks to the five ratite specimens. After application of surface semilandmarks, all surface landmarks were slid to reduce bending energy (41). Analysis of unilateral landmarks on bilaterally symmetrical structures can introduce undesirable error during superimposition (42). To mitigate these effects, all right-side semilandmarks were mirrored to the left side, and then specimens were subjected to a Procrustes alignment (43). The mirrored left-side landmarks and semilandmarks were then deleted to reduce dimensionality of the data, resulting in a final dataset of 757 aligned landmarks. See *SI Appendix, SI Methods*, for additional considerations when dealing with high-dimensional data such as these.

Phylogenetic Trees. We utilized a recent hypothesis of the phylogenetic relationships of birds based on next-generation sequencing data (21) for all comparative analyses. To generate a phylogeny containing all measured taxa for this study, we generated a composite topology following the procedure in ref. 30. This incorporates the backbone of relationships among major clades from ref. 21 along with the fine-scale species relationships from a maximum clade credibility tree generated from www.birdtree.org (44). The tree of 9,993 species was then pruned to match the 352 taxa in our dataset. Finally, our dataset contains the recently extinct *Xenicus longipes*, which is not present in the published molecular phylogenies. We substituted *X. longipes* at the position of *Xenicus gilviventris*.

Modularity Analysis. We used a likelihood-based approach (17) to evaluate the degree to which the avian skull is structured as a set of interrelated

anatomical modules. EMMLi allows between- and within-module correlations to be calculated based on user-defined models of modular organization and then evaluates the likelihood of each model. We evaluated 16 different hypotheses of the structure of modularity in the landmark configurations, ranging from 2 to 13 modules. The model with 13 modules had the highest likelihood. However, in examining the observed correlations between modules, a clear pattern becomes evident (*SI Appendix, Table S2A*). The correlation between the dorsomedial and ventrolateral margins of the naris are extremely high ($\rho = 0.73$), justifying the binning of these regions into a single module. Similarly, the pairwise correlations between all regions of both the pterygoid and quadrate are very high ($\rho = 0.54\text{--}0.95$). We therefore combined the landmarks and semilandmarks on each of these two elements into a single pterygoid-quadrate module. This resulted in a seven-module hypothesis of the organization of the skull, composed of the rostrum (dorsal surface of the premaxilla, nasal, jugal bar), cranial vault (frontal, parietal, and squamosal; anatomical terminology from ref. 39), occipital (supraoccipital, paraoccipital, basioccipital), basisphenoid, pterygoid-quadrate (ventral surface or pterygoid and articular surface of quadrate), palate (ventral surface of premaxilla and palatine), and naris (the perimeter of the external naris). Each subsequent analysis was carried out on each of the seven modules individually and also on the whole skull configuration. To test the effects of shared ancestry on trait correlations, we also carried out EMMLi analysis on the phylogenetic independent contrasts (45) of the landmark configurations. This analysis supported the same most likely model and relative strength of correlations within and among modules as the analysis of the raw data did.

1. Owen R (1863) On the *Archaeopteryx* of Von Meyer, with a description of the fossil remains of a long-tailed species from the lithographic stone of Solnhofen. *Philos Trans R Soc Lond* 153:33–47.
2. de Beer GR (1954) Archaeopteryx and evolution. *Adv Sci* 11:160–170.
3. Clarke JA, Middleton KM (2008) Mosaicism, modules, and the evolution of birds: Results from a Bayesian approach to the study of morphological evolution using discrete character data. *Syst Biol* 57:185–201.
4. Gatesy SM, Dial KP (1996) Locomotor modules and the evolution of avian flight. *Evolution* 50:331–340.
5. Cracraft J (1970) Mandible of *Archaeopteryx* provides an example of mosaic evolution. *Nature* 226:1268.
6. Balanoff AM, Smaers JB, Turner AH (2016) Brain modularity across the theropod-bird transition: Testing the influence of flight on neuroanatomical variation. *J Anat* 229: 204–214.
7. Mallarino R, et al. (2011) Two developmental modules establish 3D beak-shape variation in Darwin's finches. *Proc Natl Acad Sci USA* 108:4057–4062.
8. Abourachid A, Höfling E (2012) The legs: A key to bird evolutionary success. *J Ornithol* 153:193–198.
9. Klingenberg CP, Marugán-Lobón J (2013) Evolutionary covariation in geometric morphometric data: Analyzing integration, modularity, and allometry in a phylogenetic context. *Syst Biol* 62:591–610.
10. Kulemeyer C, Asbahr K, Gunz P, Frahnert S, Bairlein F (2009) Functional morphology and integration of corvid skulls: A 3D geometric morphometric approach. *Front Zool* 6:2.
11. Bhullar B-AS, et al. (2015) A molecular mechanism for the origin of a key evolutionary innovation, the bird beak and palate, revealed by an integrative approach to major transitions in vertebrate history. *Evolution* 69:1665–1677.
12. Bright JA, Marugán-Lobón J, Cobb SN, Rayfield EJ (2016) The shapes of bird beaks are highly controlled by nondirectional factors. *Proc Natl Acad Sci USA* 113:5352–5357.
13. Goswami A, Smaers JB, Soligo C, Polly PD (2014) The macroevolutionary consequences of phenotypic integration: From development to deep time. *Philos Trans R Soc Lond B Biol Sci* 369:20130254.
14. Goswami A, Polly PD (2010) The influence of modularity on cranial morphological disparity in carnivora and primates (Mammalia). *PLoS One* 5:e9517–e9518.
15. Marroig G, Shirai LT, Porto A, Oliveira FB, Conto V (2009) The evolution of modularity in the mammalian skull II: Evolutionary consequences. *Evol Biol* 36:136–148.
16. Randau M, Goswami A (2017) Unravelling intravertebral integration, modularity and disparity in Felidae (Mammalia). *Evol Dev* 19:85–95.
17. Goswami A, Finarelli JA (2016) EMMLi: A maximum likelihood approach to the analysis of modularity. *Evolution* 70:1622–1637.
18. Adams DC (2016) Evaluating modularity in morphometric data: Challenges with the RV coefficient and a new test measure. *Methods Ecol Evol* 7:565–572.
19. Parr WCH, et al. (2016) Cranial shape and the modularity of hybridization in dingoes and dogs: Hybridization does not spell the end for native morphology. *Evol Biol* 43: 171–187.
20. Adams DC (2014) Quantifying and comparing phylogenetic evolutionary rates for shape and other high-dimensional phenotypic data. *Syst Biol* 63:166–177.
21. Prum RO, et al. (2015) A comprehensive phylogeny of birds (Aves) using targeted next-generation DNA sequencing. *Nature* 526:569–573.
22. Maddin HC, Piekarski N, Sefton EM, Hanken J (2016) Homology of the cranial vault in birds: New insights based on embryonic fate-mapping and character analysis. *R Soc Open Sci* 3:160356.
23. Goswami A (2006) Cranial modularity shifts during mammalian evolution. *Am Nat* 168:270–280.
24. Adams DC (2014) A generalized K statistic for estimating phylogenetic signal from shape and other high-dimensional multivariate data. *Syst Biol* 63:685–697.
25. Claramunt S, Cracraft J (2015) A new time tree reveals Earth history's imprint on the evolution of modern birds. *Sci Adv* 1:e1501005.
26. Slack KE, et al. (2006) Early penguin fossils, plus mitochondrial genomes, calibrate avian evolution. *Mol Biol Evol* 23:1144–1155.
27. Ksepka DT, Stidham TA, Williamson TE (2017) Early Paleocene landbird supports rapid phylogenetic and morphological diversification of crown birds after the K-Pg mass extinction. *Proc Natl Acad Sci USA* 114:8047–8052.
28. Barker FK, Barrowclough GF, Groth JG (2002) A phylogenetic hypothesis for passerine birds: Taxonomic and biogeographic implications of an analysis of nuclear DNA sequence data. *Proc Biol Sci* 269:295–308.
29. Seki Y, Bodde SG, Meyers MA (2010) Toucan and hornbill beaks: A comparative study. *Acta Biomater* 6:331–343.
30. Cooney CR, et al. (2017) Mega-evolutionary dynamics of the adaptive radiation of birds. *Nature* 542:344–347.
31. Zusi RL, Livezey BC (2006) Variation in the os palatinum and its structural relation to the palatum osseum of birds (Aves). *Ann Carnegie Mus* 75:137–180.
32. Cuervo JJ, Moller AP (1999) Evolutionary rates of secondary sexual and non-sexual characters among birds. *Evol Ecol* 13:283–303.
33. Clarke JA, Tambussi CP, Noriega JI, Erickson GM, Ketcham RA (2005) Definitive fossil evidence for the extant avian radiation in the Cretaceous. *Nature* 433:305–308.
34. Wiley DF, et al. (2005) Evolutionary morphing. *Visualization 2005* (IEEE, Washington, DC), pp 431–438.
35. Goolsby EW (2017) Rapid maximum likelihood ancestral state reconstruction of continuous characters: A rerooting-free algorithm. *Ecol Evol* 7:2791–2797.
36. Adams DC, Otárola-Castillo E (2013) geomorph: An R package for the collection and analysis of geometric morphometric shape data. *Methods Ecol Evol* 4:393–399.
37. Wilman H, et al. (2014) EltonTraits 1.0: Species-level foraging attributes of the world's birds and mammals. *Ecology* 95:2027.
38. Finarelli JA, Flynn JJ (2006) Ancestral state reconstruction of body size in the Caniformia (Carnivora, Mammalia): The effects of incorporating data from the fossil record. *Syst Biol* 55:301–313.
39. Fabbri M, et al. (2017) The skull roof tracks the brain during the evolution and development of reptiles including birds. *Nat Ecol Evol* 1:1543–1550.
40. Schläger S (2017) Morpho and Rvcg-Shape analysis in R. *Statistical Shape and Deformation Analysis*, eds Zheng G, Li S, Székely GJ (Academic, London), pp 217–256.
41. Gunz P, Mitteroecker P, Bookstein F, Slice D (2005) Semilandmarks in three dimensions. *Modern Morphometrics in Physical Anthropology*, ed Slice DE (Springer, New York), pp 73–98.
42. Cardini A (2017) Left, right or both? Estimating and improving accuracy of one-side-only geometric morphometric analyses of cranial variation. *J Zool Syst Evol Res* 55: 1–10.
43. Rohlf FJ, Slice D (1990) Extensions of the procrustes method for the optimal superimposition of landmarks. *Syst Zool* 39:40–59.
44. Jetz W, Thomas GH, Joy JB, Hartmann K, Mooers AO (2012) The global diversity of birds in space and time. *Nature* 491:444–448.
45. Felsenstein J (1985) Phylogenies and the comparative method. *Am Nat* 125:1–15.
46. Adams DC (2013) Comparing evolutionary rates for different phenotypic traits on a phylogeny using likelihood. *Syst Biol* 62:181–192.

We also evaluated the seven-module hypothesis (Fig. 1) by calculating covariance ratios (CR) between all pairs of modules (18). There is significant modularity between all pairs of modules ($P = 0.001$, *SI Appendix, Table S3*). CR is highest between rostrum and palate modules ($CR = 0.99$); however, this value represents significant modularity compared with the distribution of CR calculated from 1,000 simulations.

Phylogenetic Signal. Phylogenetic signal was calculated for each module using the K_{mult} statistic, a method specifically designed for the challenges of working with high-dimensional landmark configurations (24).

Evolutionary Rates. The rate of evolution in each module was analyzed with BayesTraitV3 (www.evolution.rdg.ac.uk/), using principal-component scores as the input data (Figs. 3 and 4 and *SI Appendix, Figs. S1–S8*). We also calculated the multivariate rate of evolution (σ^2_{mult}) directly from the landmark data (46). See *SI Appendix, SI Methods*, for additional detail.

ACKNOWLEDGMENTS. We thank Judith White, Christine Lefevre, Chris Milensky, Steve Rogers, Ben Marks, Janet Hinshaw, Paul Sweet, Lydia Garetano, Kristof Zyskowski, and Greg Watkins-Colwell for facilitating data collection; Anne-Claire Fabre, Henry Ferguson-Gow, and Léo Botton-Divet for methodological assistance; Catherine Early for CT scanning; and Aki Watanabe, Carla Bardua, Thomas Halliday, Marcela Randau, Eve Noirault, and three anonymous reviewers for providing helpful feedback and comments. This research was funded by European Research Council Grants STG-2014-637171 (to A.G.) and SYNTHESYS FR-TAF-5635 (to R.N.F.).

Supporting Appendix:

Supplementary Methods:

Analysis of Allometry: We evaluated the strength and significance of allometric effects for each module using Procrustes ANOVA (47). Centroid size for the whole skull was used as the independent variable and the configurations of aligned landmarks for each module were used as dependent variables. For each module, the effect of skull size was significant ($p < 0.01$). However, the goodness-of-fit is very low ($R^2 < 0.18$ for all modules except the occipital, $R^2 = 0.32$), indicating that a relatively small proportion of the observed shape variation is explained by allometry. For this reason, and for consistency with recent studies (30), we did not remove allometry-related variation in subsequent analyses.

Evolutionary Rates Analysis: The rate of evolution in each module was analysed using BayesTraitsV3 (<http://www.evolution.rdg.ac.uk/>). This method uses a reversible jump Markov Chain Monte Carlo algorithm to detect the probability of shifts in the rate of evolution of a continuous trait or traits across a phylogenetic tree. Because no method currently exists for fitting and comparing evolutionary models with high-dimensional landmark data (48), we utilized Principal Component Analyses to reduce the dimensionality of the data. Separate PCAs were conducted for the landmarks comprising each module, and BayesTraits analyses were conducted on the scores from the PC axes that describe 95% of the variation for each module (Table S1). Although PC axes are uncorrelated with one another in non-phylogenetic morphospace, they are evolutionarily correlated (48). For this reason, we used the “TestCorrel” setting in BayesTraits to fit correlated multivariate evolutionary models. Five models were tested for each dataset: Brownian Motion, lambda, kappa, delta, and Ornstein–Uhlenbeck. Each analysis was allowed to run for 1,010,000 iterations and the first 10,000 iterations were deleted as the burn-in. Marginal likelihood of each model was estimated using steppingstone sampling (Table S4)(49). For each module, rate through time (Fig 1C) was summarized by dividing the phylogeny into one-million-year time bins, then computing the mean rate of all branches present in each bin and dividing by the mean rate across all time bins for that module. We also calculated evolutionary rate directly from the landmark configurations using the ‘geomorph’ R package (20, 36). This metric, σ^2_{mult} , enables evolutionary rates to be compared among modules described by high-dimensional multivariate data but assumes a Brownian Motion model of evolution (46, 50). Finally, we calculated Procrustes variance for each module as a metric of morphological disparity (36).

Additional considerations for working with high-dimensional data: Analysing high dimensional morphometric datasets such as the one utilized here require some special considerations compared to more traditional geometric morphometric data. First, our data approaches phenome-scale quantification of the cranial phenotype, but some regions of the skull were not landmarked because they cannot be consistently imaged using surface scanning technology (e.g., interorbital septum, quadratic-squamosal-otic joint). Second, applying comparative methods to high-dimensional data imposes some statistical challenges as summarized in Ref. 47, including the “curse of dimensionality:” the observation that statistical power decreases as the number of trait dimensions increases. To mitigate this effect, we randomly subsampled the complete landmark configuration to 80, 50, and 20% of the original number of landmarks, maintaining a minimum of five landmarks per module, and subjected the reduced datasets to EMMLi analysis, evaluating the likelihood of all 16 modularity hypotheses. All subsampled datasets recovered the same patterns of modularity as the full landmark configuration, demonstrating that these results are robust to the high

dimensionality of the dataset. In addition, evolutionary model comparison using extremely high-dimensional data is not possible with current techniques. Thus, dimension-reduction methods (e.g., PCA) must be used (30, 48). However, future development of more advanced tools for analyzing phenomic data will allow for evolutionary models to be fit directly to landmark configurations of this size.

A further consequence of available evolutionary modelling methods for phenotypic data is that the finding that a lambda model, rather than kappa (punctuational) or delta (early burst), has the highest likelihood for each module. This may be attributed to highly heterogenous tempo and mode of evolution. Individual subclades are likely to have evolved in a manner best approximated by different evolutionary models. Current methods for modelling multivariate evolution are suitable for detecting shifts in rate, but struggle with accurate determination of evolutionary mode (48). The development of advanced methods for model selection (e.g., a multivariate extension of fitting Lévy processes (51)) will enable us to better describe more complex patterns of phenomic evolution.

Analyses of modularity for combined landmark and semilandmark configurations of this size are also very limited, but tend to find more complex models than analysis of landmarks alone (19). It is likely that increased parameterization of models is a consequence of denser sampling of morphology, as many landmarks from a single structure will inevitably have higher correlations than a traditional landmark sampling scheme with just a few landmarks per structure. That is not simply a statistical artefact, but rather the result of better representation of morphology and the relationships among different aspects of shape. It may, however, exaggerate the modularity of a system by partitioning extremely highly correlated subregions within an overall highly integrated structure. For this reason, it is imperative to examine the results of any analysis of modularity to assess whether relationships among modules differ substantially from those within the respective modules, as we have reported here. Identification of phenotypic modules also provides an additional benefit to the analysis of high-density phenomic data as reconstructing macroevolutionary patterns separately in each supported module reduces trait data dimensionality without compromising the accurate representation of complex morphology.

Supplementary References:

47. Collyer ML, Sekora DJ, Adams DC (2015) A method for analysis of phenotypic change for phenotypes described by high-dimensional data. *Heredity (Edinb)* 115:357–365.
48. Adams DC, Collyer ML (2017) Multivariate Phylogenetic Comparative Methods: Evaluations, Comparisons, and Recommendations. *Syst Biol* Accepted. Available at: <https://doi.org/10.1093/sysbio/syx055>
49. Xie W, Lewis PO, Fan Y, Kuo L, Chen MH (2011) Improving marginal likelihood estimation for bayesian phylogenetic model selection. *Syst Biol* 60(2):150–160.
50. Adams DC (2013) Comparing Evolutionary Rates for Different Phenotypic Traits on a Phylogeny Using Likelihood. *Syst Biol* 62(2):181–192.
51. Duchen P, et al. (2017) Inference of evolutionary jumps in large phylogenies using Lévy processes. *Syst Biol*:syx028.
52. Iwaniuk AN, Dean KM, Nelson JE (2005) Interspecific allometry of the brain and brain regions in parrots (Psittaciformes): Comparisons with other birds and primates. *Brain Behav Evol* 65(1):40–59.

Table S1: Multivariate Evolutionary Signal and Rate

Module	K_{mult}	σ^2_{mult}	Number of PC Axes Describing 95% of Cumulative Variance
Rostrum	0.58	3.31E-07	14
Vault	0.55	2.82E-07	13
Basisphenoid	0.56	7.16E-08	8
Palate	0.65	2.98E-07	11
Pterygoid-quadratae	0.66	1.15E-07	7
Naris	0.48	3.43E-07	5
Occiput	0.59	1.23E-07	9
Whole Skull	0.59	2.33E-07	29

Table S2: EMMLi Results: Between- and Within-Module Correlations

A: Thirteen Module Model:

B: Seven Module Model

Table S3: Covariance Ratio Results

	Rostrum	Vault	Basisphenoid	Palate	Pterygoid-Quadratae	Naris
Vault	0.85					
Basisphenoid	0.73	0.75				
Palate	0.99	0.86	0.72			
Jaw Articulation	0.79	0.76	0.79	0.75		
Naris	0.70	0.44	0.36	0.60	0.42	
Occipital	0.77	0.90	0.78	0.79	0.68	0.38

Table S4: BayesTraits Results: Marginal Log Likelihood For Each Model

Evolutionary Model	Rostrum	Vault	Basisphenoid	Palate	Pterygoid-Quadratae	Naris	Occiput	Whole Skull
BM	-18158.5	-16313.6	-8463.5	-14369.5	-8118.5	-5735.9	-10468.0	-39250.4
OU	-18141.8	-16304.3	-8452.3	-14375.2	-8115.7	-5742.2	-10453.6	-39248.1
BM + Lambda	-18107.4	-16274.1	-8426.8	-14328.1	-8070.5	-5720.7	-10410.4	-39160.3
BM + Kappa	-18168.5	-16325.3	-8463.0	-14360.1	-8106.7	-5733.8	-10466.3	-39291.4
BM + Delta	-18162.7	-16316.1	-8470.8	-14376.4	-8109.0	-5735.2	-10475.3	-39282.0

Supplementary Figures:

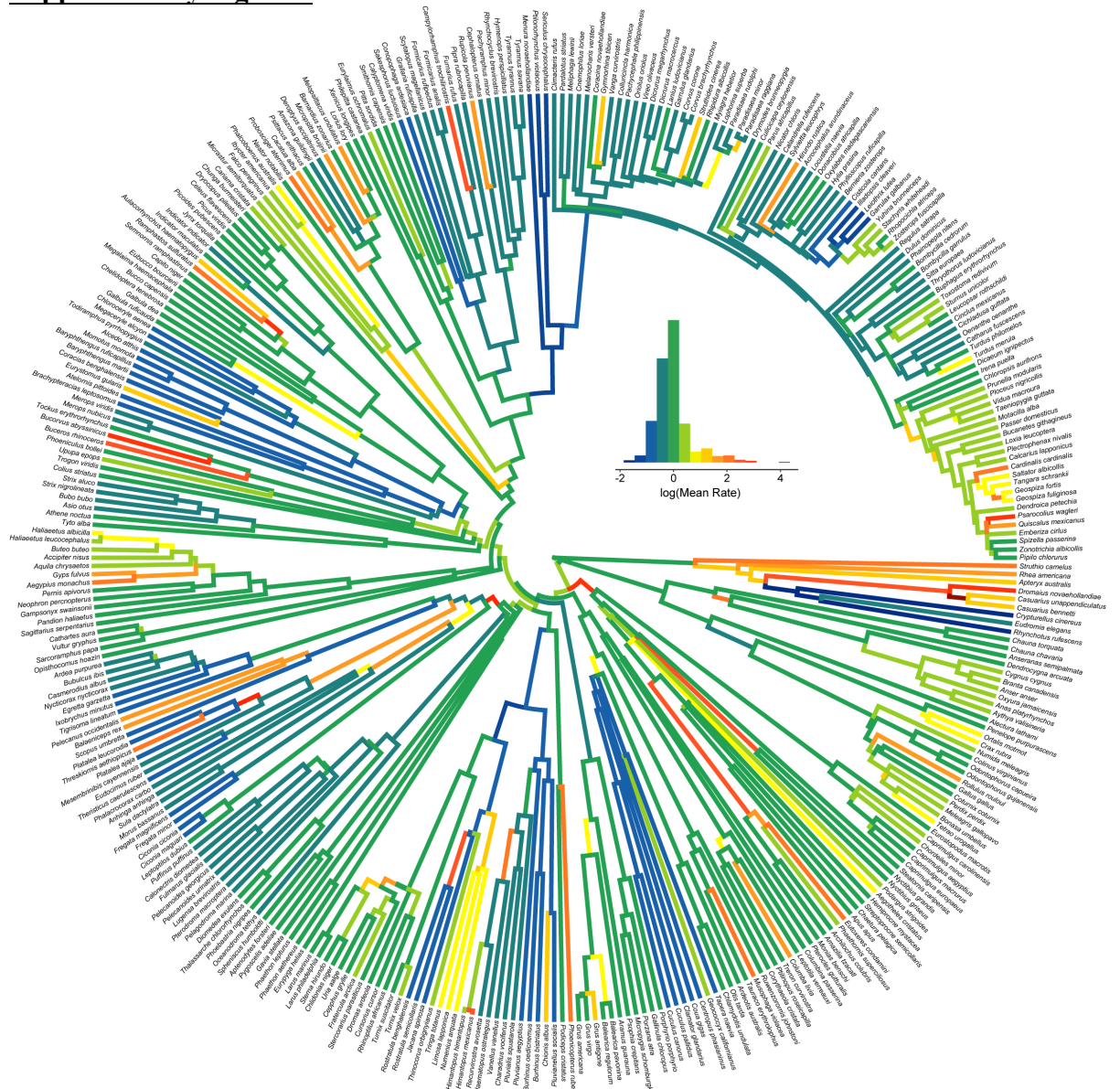


Figure S1: Rostrum Module Rates. Note the punctuated burst of rostrum evolution at the common ancestor of *Geospiza fortis* and *Geospiza fuliginosa* (examples of Darwin's finches), supporting rapid phenotypic diversification in this radiation.

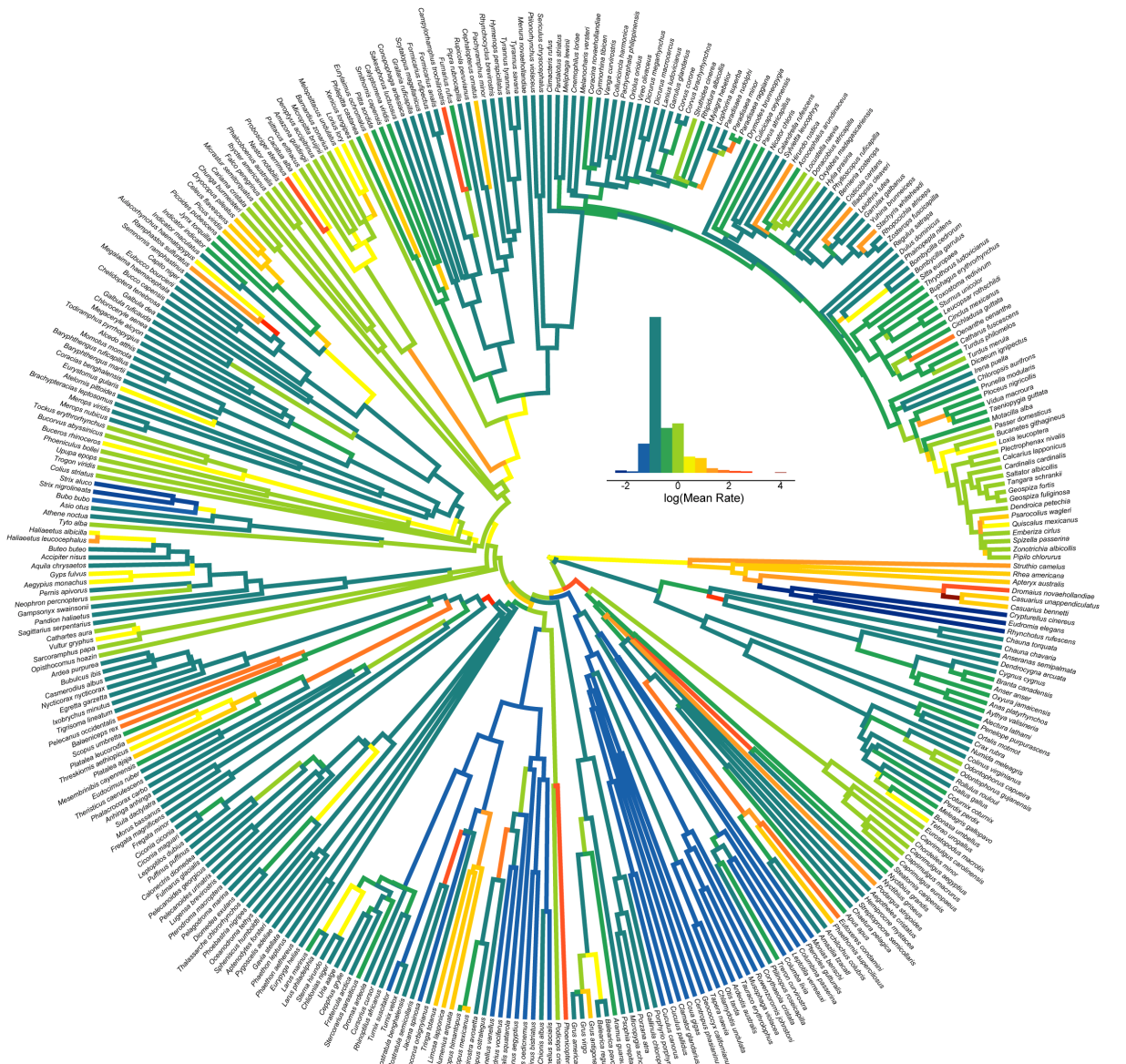


Figure S2: Palate Module Rates The palate evolves quickly in clades including Psittaciformes, Bucerotiformes, Passeroidea, ‘Caprimulgiformes’, Threskiornithidae, Picidae, and Ramphastidae, as well as isolated taxa such as *Grus antigone*, *Haliaeetus albicilla*, and *Campylorhamphus trochilirostris*. The divergent palatal morphology of ratites is reconstructed as evolving extremely fast whereas that of Tinamiformes appear to evolve extremely slowly.

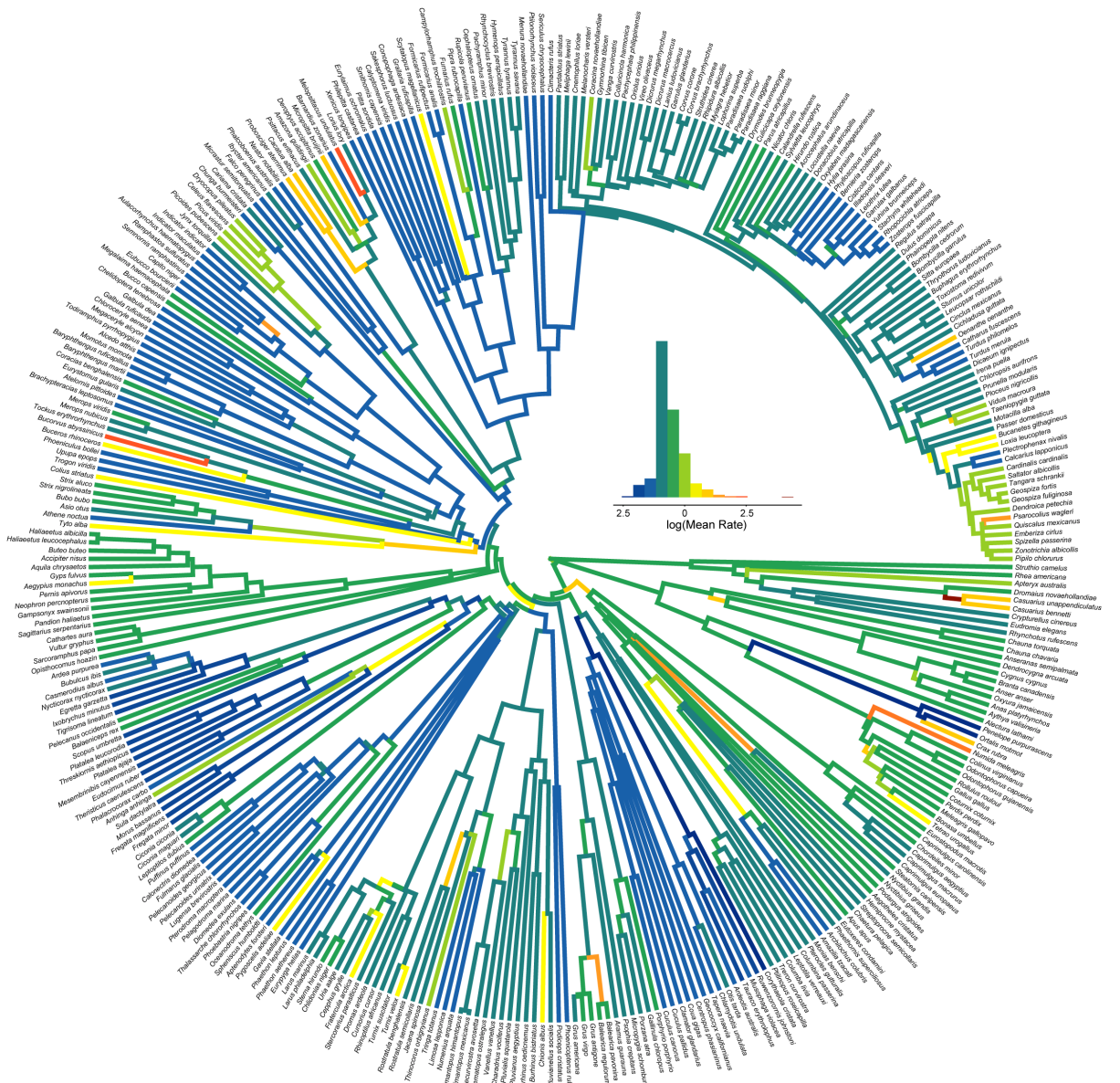


Figure S3: Cranial Vault Module Rates. Species with cranial ornaments evolve quickly. There are also bursts of rapid evolution at the origin of Strigiformes, Strisores, and Trochilidae. Despite the high encephalization quotient of parrots (52), only a subset of Psittaciformes show elevated rates in this module. Some additional lineages with elevated rates include *Balearica*, *Rostratula*, and *Psarocolius wagleri*.

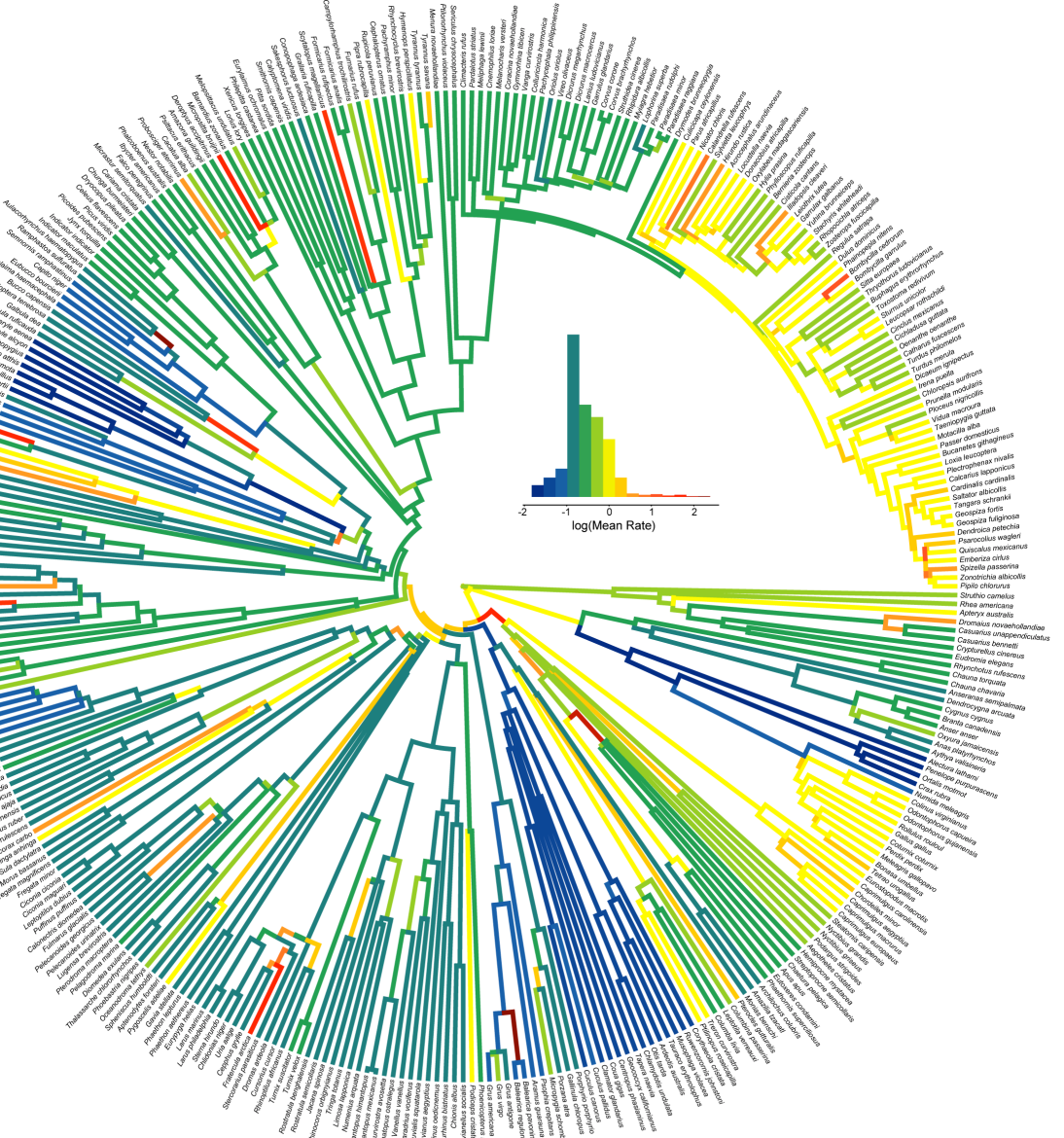


Figure S4: Occipital Module Rates. Passeri exhibits high rates throughout, although rates are variable among lineages within the clade. There are a number of punctuated evolution events, occurring primarily at the early divergences near the root of the tree. Sustained high rates are observed in Caprimulgidae and Phasianidae. *Fratercula artica*, *Gyps fulvus*, *Accipiter nisus*, *Dromaius novaehollandiae*, *Balearica*, *Scytalopus magellanicus*, *Micropsitta bruijnii*, *Probosciger aterrimus*, and many other species also have high rates of occipital evolution.

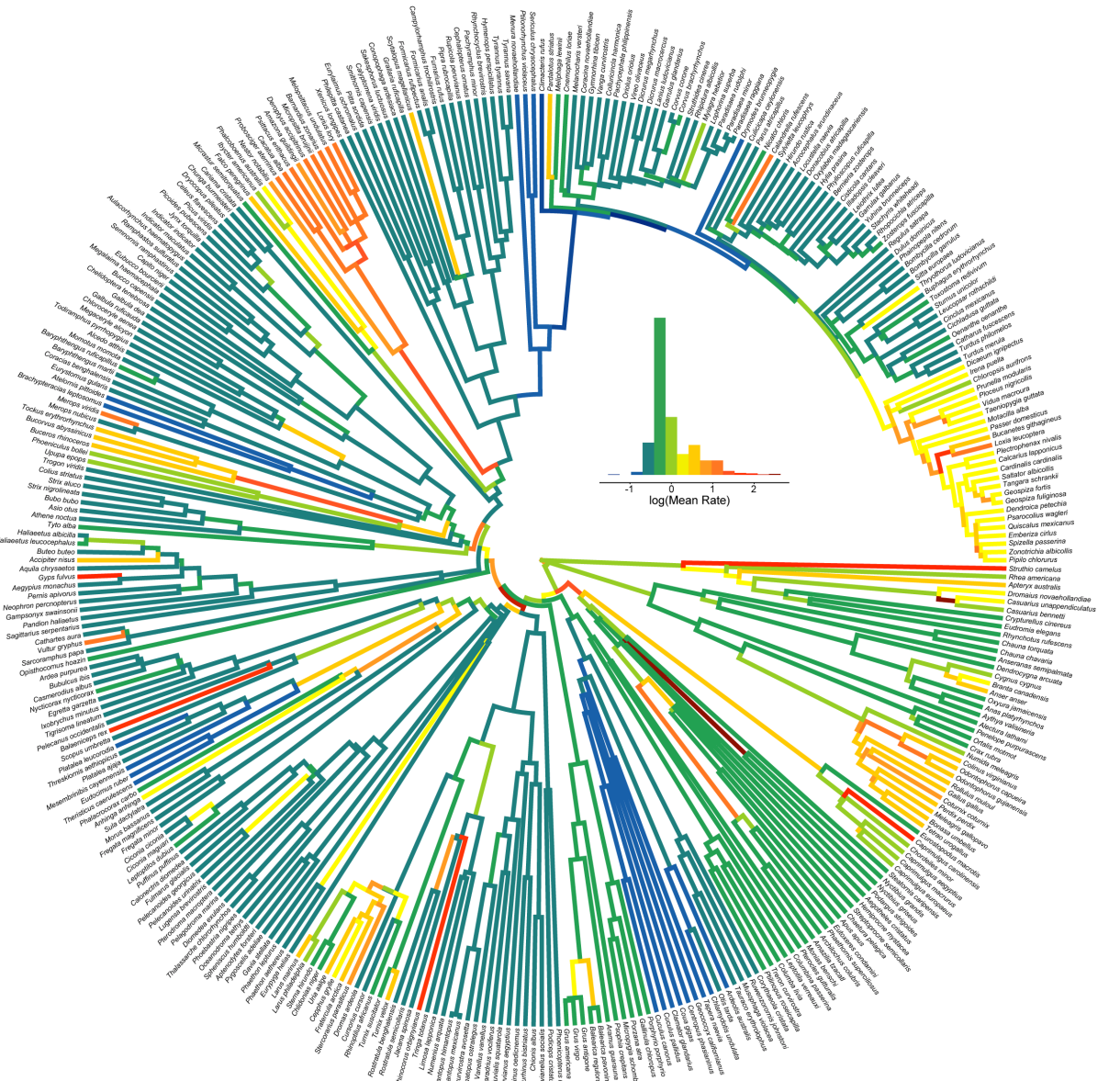


Figure S5: Pterygoid-quadrata Module Rates. Phasianidae, Passeroidea, Psittaciformes, and Bucerotiformes experience a high rates of evolution for this module. Isolated bursts of rapid evolution are observed throughout the tree, most notably at the origin of Aequorlitornithes, Strisores, Trochilidae, and *Nyctibius*.

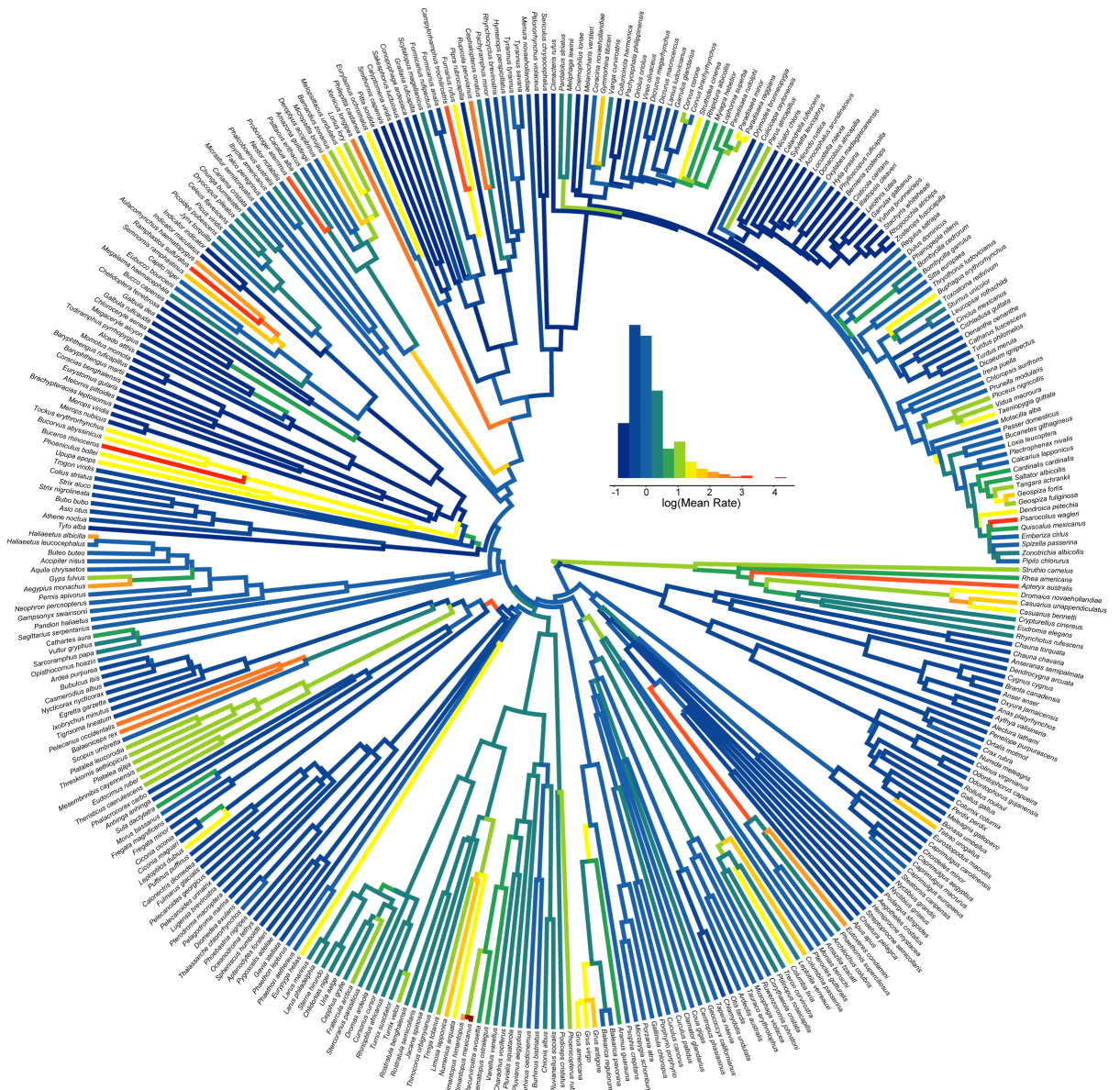


Figure S6: Naris Module Rates. The fastest rates of evolution are observed in clades with extremely posteriorly oriented nares (e.g., Bucerotidae, Ramphastidae *Pelecanus*, *Balaeniceps*). High rates are observed elsewhere, including *Apteryx australis*, *Himantopus*, *Xenicus longipes*, *Psarocolius wagleri*, *Campylorhamphus trochilirostris*, *Rupicola peruvianus*, and others.

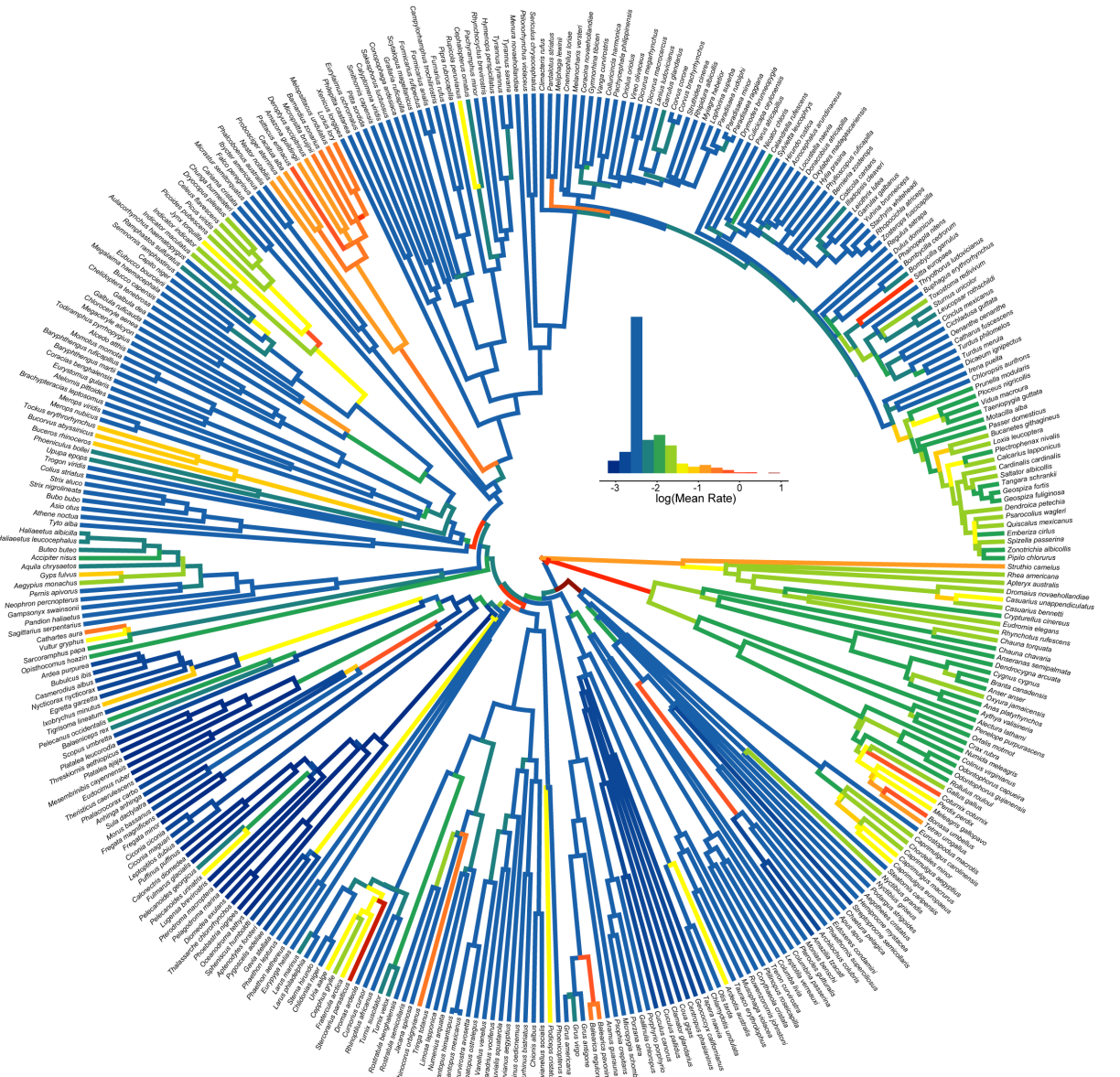


Figure S7: Basisphenoid Module Rates: Bursts of basisphenoid evolution took place at the origin of Strisores, Aequorlitorinthes, Picidae, Trochilidae, and in several members of Phasianidae. Sustained high rates are observed in Phasianidae and Psittaciformes. Isolated branches with high rates include *Stercorarius parasiticus*, *Balearica*, *Cathartes aura*, and *Sitta europaea*.

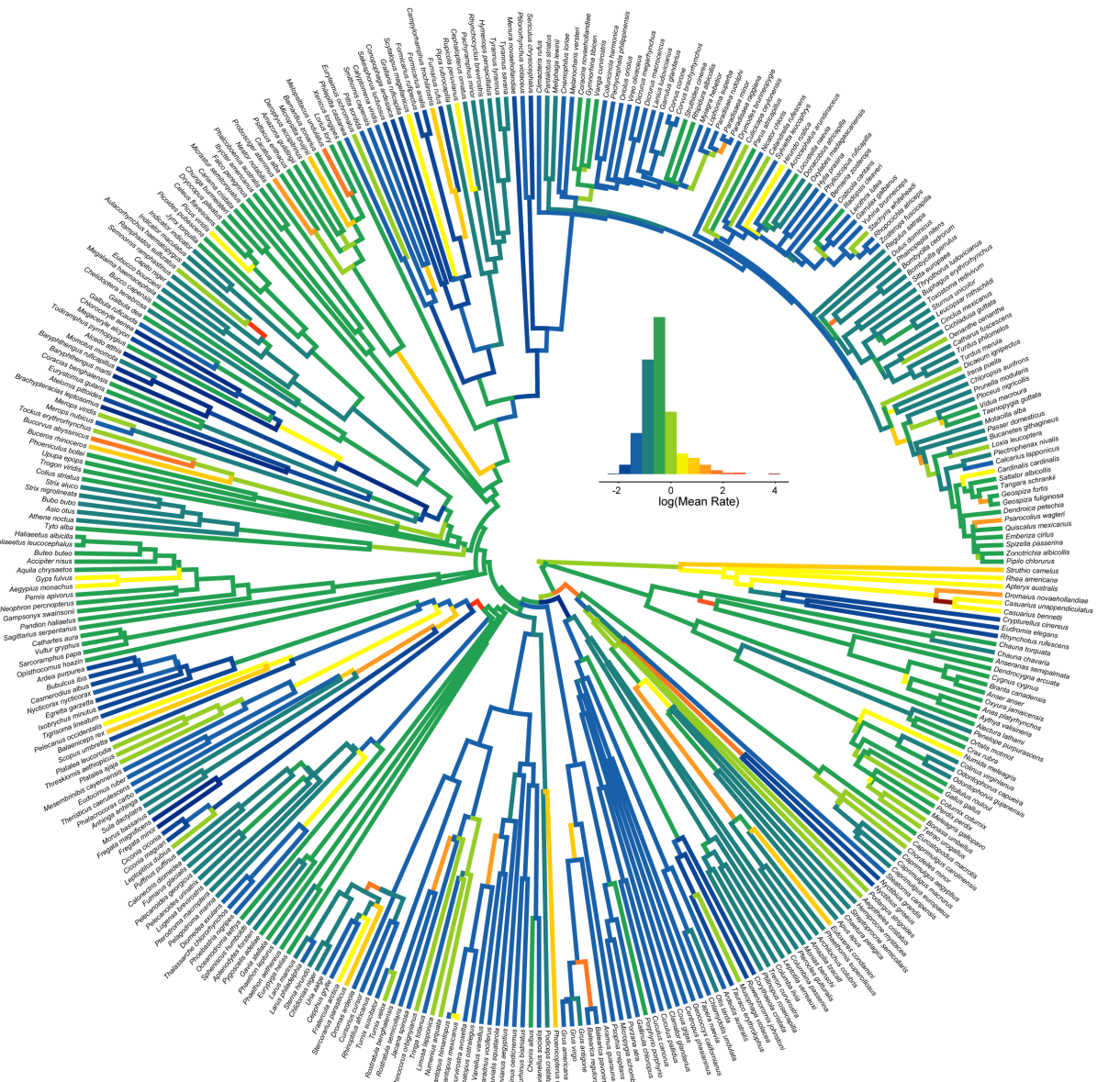


Figure S8: Whole Skull Rates. The root of Strisores and Pelecaniformes each have high rates near the initial diversification of Neoaves and there are high rates at the root of Anatidae, Apodidae, Trochilidae, Lari, Threskiornithidae, Suliformes, Gruidae+Aramidae, Bucerotiformes, and Psittaciformes). Shifts in evolutionary rates for the whole skull occur on branches that also experience rate changes in either the rostrum (e.g., *Phoenicopterus*) or cranial ornaments (e.g., *Balearica*). Thus, modelling phenotypic change through time in the whole skull may be strongly influenced by change occurring in these regions, obscuring rate changes in other parts of the skull.

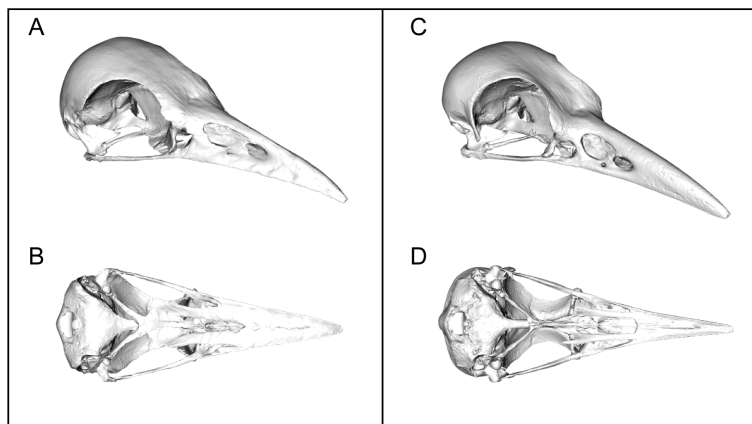


Figure S9: Hypothesized ancestral cranial phenotype in dorsal oblique (A) and ventral (B) view compared to the specimen it most closely resembles, *Vanga curvirostris* (MNHN 2017-254), dorsal oblique (C) and ventral (D) view.

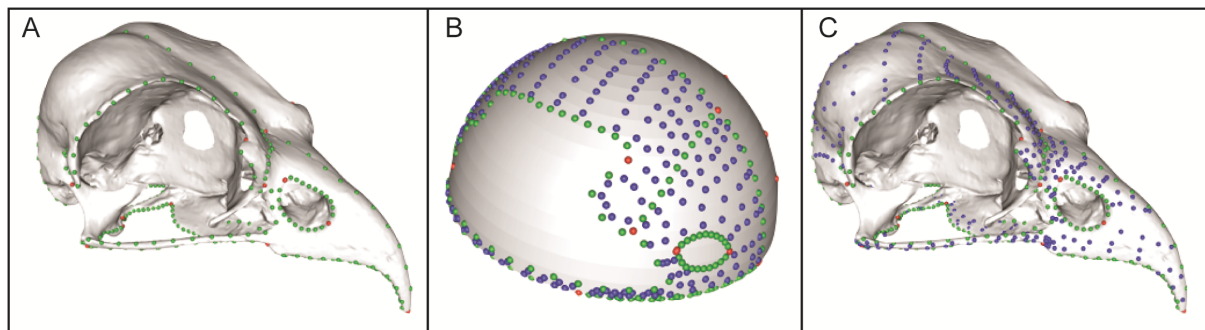


Figure S10: Semi-Automated Landmarking Procedure. Landmarks (red) and sliding semi-landmarks (green) are placed manually on each skull (A). Corresponding landmarks, semilandmarks, and surface landmarks (blue) are placed on a simplified template (B). An automated procedure is used to apply surface landmarks from the template to each specimen, generating the full landmark configuration (C)

Supplemental Data File 1 - Taxonomic Sampling List			
Family (from IOC World Bird List)	Species	Collection	Specimen Number
Struthionidae	<i>Struthio camelus</i>	MNHN	1908160
Rheidae	<i>Rhea americana</i>	MNHN	1878730
Casuariidae	<i>Casuarius bennetti</i>	NHMUK	1950231
Casuariidae	<i>Casuarius unappendiculatus</i>	USNM	489302
Dromaiidae	<i>Dromaius novaehollandiae</i>	USNM	500379
Apterygidae	<i>Apteryx australis</i>	YPM	110849
Tinamidae	<i>Crypturellus cinereus</i>	USNM	428833
Tinamidae	<i>Rhynchos rufescens</i>	NHMUK	S-1952-1-24
Tinamidae	<i>Nothoprocta ornata</i>	USNM	620751
Tinamidae	<i>Eudromia elegans</i>	USNM	345094
Cracidae	<i>Ortalix motmot</i>	USNM	621705
Cracidae	<i>Penelope purpurascens</i>	USNM	288719
Cracidae	<i>Crax rubra</i>	NHMUK	18537127
Megapodiidae	<i>Alectura lathami</i>	MNHN	18811115
Phasianidae	<i>Perdix perdix</i>	USNM	553824
Phasianidae	<i>Coturnix coturnix</i>	USNM	603427
Phasianidae	<i>Rollulus rouloul</i>	NHMUK	1891-7-20-87
Phasianidae	<i>Gallus gallus</i>	MNHN	1880207
Phasianidae	<i>Tetrao urogallus</i>	YPM	102910
Phasianidae	<i>Bonasa umbellus</i>	YPM	104640
Phasianidae	<i>Meleagris gallopavo</i>	USNM	346978
Numididae	<i>Numida meleagris</i>	USNM	290390
Odontophoridae	<i>Colinus virginianus</i>	NHMUK	S-1994-64-2
Odontophoridae	<i>Odontophorus gujanensis</i>	USNM	621708
Odontophoridae	<i>Odontophorus capueira</i>	MNHN	1868-180
Anhimidae	<i>Chauna chavaria</i>	NHMUK	S-1954-3-3
Anhimidae	<i>Chauna torquata</i>	USNM	347352
Anseranatidae	<i>Anseranas semipalmata</i>	USNM	347638
Anatidae	<i>Dendrocygna arcuata</i>	NHMUK	20122804
Anatidae	<i>Oxyura jamaicensis</i>	NHMUK	S-2004-18-1
Anatidae	<i>Cygnus cygnus</i>	MNHN	1893482
Anatidae	<i>Anser anser</i>	USNM	291065
Anatidae	<i>Branta canadensis</i>	USNM	488182
Anatidae	<i>Anas platyrhynchos</i>	USNM	631964
Anatidae	<i>Aythya valisineria</i>	NHMUK	S-2002471
Turnicidae	<i>Turnix suscitator</i>	USNM	562147
Turnicidae	<i>Turnix velox</i>	AMNH	9658
Indicatoridae	<i>Indicator maculatus</i>	USNM	631581
Indicatoridae	<i>Indicator indicator</i>	USNM	430329
Picidae	<i>Jynx torquilla</i>	USNM	602914
Picidae	<i>Picoides pubescens</i>	USNM	498607
Picidae	<i>Celeus flavescens</i>	AMNH	4212
Picidae	<i>Dryocopus pileatus</i>	FMNH	349048
Picidae	<i>Picus viridis</i>	AMNH	31676
Ramphastidae	<i>Megalaima haemacephala</i>	USNM	613080
Ramphastidae	<i>Capito niger</i>	FMNH	290503
Ramphastidae	<i>Eubucco bourcierii</i>	USNM	560025

Ramphastidae	<i>Semnornis ramphastinus</i>	USNM	346963
Ramphastidae	<i>Aulacorhynchus haematopygus</i>	AMNH	27846
Ramphastidae	<i>Ramphastos sulfuratus</i>	USNM	612339
Galbulidae	<i>Galbula ruficauda</i>	AMNH	25635
Galbulidae	<i>Galbula dea</i>	USNM	623088
Bucconidae	<i>Bucco capensis</i>	USNM	621739
Bucconidae	<i>Chelidoptera tenebrosa</i>	USNM	622945
Bucerotidae	<i>Tockus erythrorhynchus</i>	USNM	322992
Bucerotidae	<i>Buceros rhinoceros</i>	USNM	346727
Bucorvidae	<i>Bucorvus abyssinicus</i>	MNHN	1884-437
Upupidae	<i>Upupa epops</i>	NHMUK	S-1968-4-2
Phoeniculidae	<i>Phoeniculus bollei</i>	AMNH	4232
Trogonidae	<i>Trogon viridis</i>	USNM	561286
Coraciidae	<i>Coracias benghalensis</i>	USNM	343284
Coraciidae	<i>Eurystomus gularis</i>	USNM	292414
Brachyptaciidae	<i>Brachyptacias leptosomus</i>	FMNH	438658
Brachyptaciidae	<i>Atelornis pittoides</i>	FMNH	438663
Momotidae	<i>Baryphthengus martii</i>	USNM	614002
Momotidae	<i>Baryphthengus ruficapillus</i>	USNM	428200
Momotidae	<i>Momotus momota</i>	USNM	344673
Alcedinidae	<i>Alcedo atthis</i>	YPM	102931
Alcedinidae	<i>Todiramphus pyrrhopygius</i>	NHMUK	S-1969-4-43
Alcedinidae	<i>Megacyrle alcyon</i>	USNM	502300
Alcedinidae	<i>Chloroceryle aenea</i>	USNM	623157
Meropidae	<i>Merops viridis</i>	NHMUK	S-1969-1-46
Meropidae	<i>Merops nubicus</i>	USNM	322454
Coliidae	<i>Colius striatus</i>	USNM	558542
Cuculidae	<i>Clamator glandarius</i>	USNM	431797
Cuculidae	<i>Cuculus canorus</i>	USNM	490322
Cuculidae	<i>Cuculus pallidus</i>	NHMUK	1966-50-34
Cuculidae	<i>Coua gigas</i>	FMNH	360040
Cuculidae	<i>Centropus phasianinus</i>	MNHN	A-4173
Cuculidae	<i>Tapera naevia</i>	UMMZ	222,217
Cuculidae	<i>Geococcyx californianus</i>	USNM	610961
Opisthocomidae	<i>Opisthocomus hoazin</i>	YPM	109944
Psittacidae	<i>Probosciger aterrimus</i>	USNM	346724
Psittacidae	<i>Cacatua alba</i>	USNM	557129
Psittacidae	<i>Lorius lory</i>	USNM	557119
Psittacidae	<i>Nestor notabilis</i>	USNM	19876
Psittacidae	<i>Micropsitta bruijnii</i>	AMNH	28102
Psittacidae	<i>Barnardius zonarius</i>	AMNH	29922
Psittacidae	<i>Melopsittacus undulatus</i>	YPM	102222
Psittacidae	<i>Psittacus erithacus</i>	MNHN	1967116
Psittacidae	<i>Anodorhynchus leari</i>	MNHN	1997431
Psittacidae	<i>Amazona guildingii</i>	USNM	613763
Psittacidae	<i>Deroptyus accipitrinus</i>	FMNH	106399
Apodidae	<i>Streptoprocne semicollaris</i>	USNM	489351
Apodidae	<i>Chaetura pelagica</i>	USNM	492655
Apodidae	<i>Apus apus</i>	YPM	1023863
Hemiprocnidae	<i>Hemiprocne mystacea</i>	AMNH	6982

Trochilidae	Phaethornis superciliosus	FMNH	386765
Trochilidae	Eutoxeres condamini	FMNH	291752
Trochilidae	Amazilia tzacatl	USNM	613408
Trochilidae	Archilochus colubris	NHMUK	S-2001.27.4
Musophagidae	Tauraco erythrolophus	AMNH	27414
Musophagidae	Ruwenzorornis johnstoni	FMNH	355262
Musophagidae	Musophaga violacea	FMNH	104075
Musophagidae	Corythaeola cristata	AMNH	24784
Tytonidae	Tyto alba	NHMUK	S-2014-4-71
Strigidae	Bubo bubo	USNM	610383
Strigidae	Strix aluco	NHMUK	S-1975-49-3
Strigidae	Strix nigrolineata	USNM	613976
Strigidae	Athene noctua	USNM	490358
Strigidae	Asio otus	MNHN	1997-457
Aegothelidae	Aegotheles cristatus	USNM	620228
Podargidae	Podargus strigoides	USNM	632131
Steatornithidae	Steatornis caripensis	USNM	560206
Nyctibiidae	Nyctibius grandis	USNM	623085
Nyctibiidae	Nyctibius griseus	USNM	610497
Caprimulgidae	Eurostopodus macrotis	USNM	431310
Caprimulgidae	Chordeiles minor	YPM	109237
Caprimulgidae	Caprimulgus carolinensis	YPM	144277
Caprimulgidae	Caprimulgus europaeus	USNM	603601
Caprimulgidae	Caprimulgus aegyptius	USNM	641346
Caprimulgidae	Caprimulgus macrurus	USNM	557180
Columbidae	Columba livia	YPM	107622
Columbidae	Columbina passerina	USNM	554675
Columbidae	Leptotila verreauxi	FMNH	104057
Columbidae	Treron curvirostra	MNHN	1884-2475
Columbidae	Ptilinopus roseicapilla	MNHN	1888-34
Eurypygidae	Eurypyga helias	MNHN	1869-396
Otididae	Otis tarda	USNM	289732
Otididae	Ardeotis australis	UMMZ	211,267
Otididae	Chlamydotis undulata	NHMUK	S-2010-5-2
Gruidae	Balearica pavonina	MNHM	1906-75
Gruidae	Balearica regulorum	USNM	637581
Gruidae	Grus antigone	NHMUK	S-1952-2-149
Gruidae	Grus virgo	MNHM	1877-660
Gruidae	Grus americana	USNM	623326
Aramidae	Aramus guarauna	USNM	635727
Psophiidae	Psophia crepitans	MNHN	2013-314
Cariamidae	Cariama cristata	NHMUK	1853-7-12-8
Cariamidae	Chunga burmeisteri	FMNH	106731
Rallidae	Micropygia schomburgkii	USNM	639367
Rallidae	Porzana atra	USNM	562787
Rallidae	Porphyrio porphyrio	MNHN	1909-511
Rallidae	Gallinula chloropus	NHMUK	S-1981-13-35
Mesitornithidae	Monias benschi	USNM	290927
Pteroclididae	Pterocles gutturalis	USNM	430847
Thinocoridae	Thinocorus orbignyanus	USNM	637907

Scolopacidae	<i>Limosa lapponica</i>	MNHN	1997-414
Scolopacidae	<i>Numenius arquata</i>	NHMUK	S-1977-21-1
Scolopacidae	<i>Tringa totanus</i>	YPM	11514
Rostratulidae	<i>Rostratula benghalensis</i>	USNM	613017
Rostratulidae	<i>Rostratula semicollaris</i>	USNM	612032
Jacanidae	<i>Jacana spinosa</i>	USNM	554280
Chionidae	<i>Chionis albus</i>	NHMUK	S-1973-66-85
Chionidae	<i>Pluvianellus socialis</i>	AMNH	17700
Burhinidae	<i>Burhinus oedicnemus</i>	MNHN	1877-333
Burhinidae	<i>Burhinus bistriatus</i>	USNM	621089
Haematopodidae	<i>Haematopus ostralegus</i>	MNHN	ME-3752
Recurvirostridae	<i>Himantopus himantopus</i>	MNHN	1880-271
Recurvirostridae	<i>Himantopus mexicanus</i>	USNM	635762
Recurvirostridae	<i>Recurvirostra avosetta</i>	NHMUK	1954-26-1
Charadriidae	<i>Pluvialis squatarola</i>	YPM	108400
Charadriidae	<i>Charadrius vociferus</i>	USNM	553645
Charadriidae	<i>Vanellus vanellus</i>	MNHN	1931-195
Dromadidae	<i>Dromas ardeola</i>	NHMUK	S-1957-7-11
Glareolidae	<i>Pluvianus aegyptius</i>	AMNH	24771
Glareolidae	<i>Rhinoptilus africanus</i>	USNM	431520
Glareolidae	<i>Cursorius cursor</i>	USNM	603507
Stercorariidae	<i>Stercorarius parasiticus</i>	USNM	502330
Laridae	<i>Larus marinus</i>	CM	5075
Laridae	<i>Larus philadelphia</i>	YPM	103857
Laridae	<i>Sterna hirundo</i>	NHMUK	S-1975-65-3
Laridae	<i>Chlidonias niger</i>	USNM	499661
Alcidae	<i>Uria aalge</i>	YPM	111991
Alcidae	<i>Cephus grylle</i>	USNM	612213
Alcidae	<i>Fratercula arctica</i>	MNHN	1888-339
Accipitridae	<i>Pandion haliaetus</i>	USNM	623422
Accipitridae	<i>Pernis apivorus</i>	MNHN	1997-309
Accipitridae	<i>Gampsonyx swainsonii</i>	USNM	622231
Accipitridae	<i>Haliaeetus albicilla</i>	USNM	292774
Accipitridae	<i>Haliaeetus leucocephalus</i>	MNHN	A-4056
Accipitridae	<i>Neophron percnopterus</i>	USNM	17835
Accipitridae	<i>Gyps fulvus</i>	MNHN	1995-160
Accipitridae	<i>Aegypius monachus</i>	AMNH	1939
Accipitridae	<i>Accipiter nisus</i>	USNM	344423
Accipitridae	<i>Buteo buteo</i>	NHMUK	S-1972-11-59
Accipitridae	<i>Aquila chrysaetos</i>	MNHN	1930-152
Accipitridae	<i>Sagittarius serpentarius</i>	AMNH	1306
Falconidae	<i>Micrastur semitorquatus</i>	USNM	245788
Falconidae	<i>Ibycter americanus</i>	YPM	139300
Falconidae	<i>Phalcoboenus australis</i>	USNM	490979
Falconidae	<i>Falco peregrinus</i>	USNM	491265
Podicipedidae	<i>Podiceps cristatus</i>	USNM	560594
Phaethontidae	<i>Phaethon aethereus</i>	USNM	18555
Phaethontidae	<i>Phaethon lepturus</i>	NHMUK	1898-91-676
Sulidae	<i>Morus bassanus</i>	MNHN	199018
Sulidae	<i>Sula dactylatra</i>	NHMUK	S-1975-3-71

Anhingidae	Anhinga anhinga	CM	26
Phalacrocoracidae	Phalacrocorax carbo	USNM	18851
Ardeidae	Tigrisoma lineatum	USNM	631043
Ardeidae	Ixobrychus minutus	USNM	603399
Ardeidae	Nycticorax nycticorax	USNM	501635
Ardeidae	Egretta garzetta	USNM	430820
Ardeidae	Ardea purpurea	MNHN	1997-225
Ardeidae	Casmerodius albus	USNM	610600
Ardeidae	Bubulcus ibis	MNHN	1997-208
Scopidae	Scopus umbretta	NHMUK	1897-5-10-38
Phoenicopteridae	Phoenicopterus ruber	MNHN	1882-206
Threskiornithidae	Eudocimus ruber	USNM	322060
Threskiornithidae	Theristicus caerulescens	USNM	635755
Threskiornithidae	Mesembrinibis cayennensis	USNM	562523
Threskiornithidae	Threskiornis aethiopicus	USNM	558414
Threskiornithidae	Platalea leucorodia	MNHN	ME48
Threskiornithidae	Platalea ajaja	MNHN	1884-2571
Balaenicipitidae	Balaeniceps rex	USNM	344963
Pelecanidae	Pelecanus occidentalis	USNM	489428
Cathartidae	Cathartes aura	USNM	17872
Cathartidae	Vultur gryphus	NHMUK	S-1956-1-81
Cathartidae	Sarcoramphus papa	MNHN	A4002-IV/188
Ciconiidae	Ciconia maguari	NHMUK	S-1955-5-2
Ciconiidae	Ciconia ciconia	MNHN	187979
Ciconiidae	Leptoptilos dubius	USNM	225988
Fregatidae	Fregata magnificens	USNM	610592
Fregatidae	Fregata minor	MNHN	1997-180
Spheniscidae	Aptenodytes forsteri	UMMZ	216,161
Spheniscidae	Pygoscelis adeliae	NHMUK	S-1966-42
Spheniscidae	Spheniscus humboldti	MNHN	1965-162
Gaviidae	Gavia stellata	USNM	561404
Procellariidae	Fulmarus glacialis	NHMUK	1898-71-21
Procellariidae	Lugensa brevirostris	MNHN	2004-378
Procellariidae	Pterodroma macroptera	USNM	500654
Procellariidae	Calonectris diomedea	MNHN	2004-413
Procellariidae	Puffinus puffinus	MNHN	1997-170
Pelecanoididae	Pelecanoides georgicus	AMNH	3232
Pelecanoididae	Pelecanoides urinatrix	NHMUK	S-1916-1-21
Diomedeidae	Diomedea exulans	NHMUK	1848-8-31-36
Diomedeidae	Phoebastria nigripes	USNM	630953
Diomedeidae	Thalassarche chlororhynchos	YPM	102976
Hydrobatidae	Pelagodroma marina	USNM	614205
Hydrobatidae	Oceanodroma tethys	USNM	614199
Acanthisittidae	Xenicus gilviventris	NHMUK	S-1972-1-108
Pittidae	Pitta sordida	USNM	432055
Eurylaimidae	Smithornis capensis	FMNH	444067
Eurylaimidae	Eurylaimus ochromalus	YPM	104081
Eurylaimidae	Calyptomena viridis	UMMZ	218,090
Philepittidae	Philepitta castanea	FMNH	393177
Tyrannidae	Rhynchocyclus brevirostris	YPM	144521

Tyrannidae	Hymenops perspicillatus	YPM	101109
Tyrannidae	Tyrannus savana	USNM	635850
Tyrannidae	Tyrannus tyrannus	AMNH	31397
Cotingidae	Pachyramphus minor	NHMUK	1891.7.20.308
Cotingidae	Cephalopterus ornatus	FMNH	106996
Cotingidae	Rupicola peruvianus	YPM	109149
Pipridae	Pipra rubrocincta	YPM	105741
Thamnophilidae	Sakesphorus luctuosus	USNM	562278
Furnariidae	Furnarius rufus	YPM	103236
Dendrocolaptidae	Campylorhamphus trochilirostris	FMNH	321456
Formicariidae	Formicarius analis	USNM	614119
Formicariidae	Formicarius rufigularis	USNM	559999
Formicariidae	Grallaria ruficapilla	AMNH	24122
Conopophagidae	Conopophaga ardesiaca	FMNH	322380
Rhinocryptidae	Scytalopus magellanicus	AMNH	24350
Climacteridae	Climacteris rufus	AMNH	29997
Menuridae	Menura novaehollandiae	USNM	632118
Ptilonorhynchidae	Sericulus chrysocephalus	FMNH	106327
Ptilonorhynchidae	Ptilonorhynchus violaceus	USNM	428269
Meliphagidae	Meliphaga lewinii	MNHN	A4476
Pardalotidae	Pardalotus striatus	NHMUK	S-1966-51-192
Petroicidae	Drymodes brunneopygia	AMNH	29949
Irenidae	Irena puella	FMNH	104162
Chloropseidae	Chloropsis aurifrons	FMNH	1042982
Laniidae	Lanius ludovicianus	USNM	554039
Vireonidae	Vireo olivaceus	AMNH	31488
Corcoracidae	Struthidea cinerea	USNM	224841
Pachycephalidae	Pachycephala philippinensis	FMNH	392304
Colluricinclidae	Colluricincla harmonica	NHMUK	S-1966-51-171
Corvidae	Garrulus glandarius	MNHN	1931-254
Corvidae	Corvus brachyrhynchos	USNM	553267
Corvidae	Corvus corone	NHMUK	S-1976-271
Cnemophilidae	Cnemophilus loriae	YPM	105212
Paradisaeidae	Lophorina superba	CM	4964
Paradisaeidae	Paradisaea minor	FMNH	104462
Paradisaeidae	Paradisaea raggiana	USNM	500630
Paradisaeidae	Paradisaea rudolphi	USNM	321104
Cracticidae	Gymnorhina tibicen	USNM	632142
Oriolidae	Oriolus oriolus	FMNH	369196
Campephagidae	Coracina novaehollandiae	CM	S-15217
Rhipiduridae	Rhipidura albicollis	NHMUK	S-1969-1-179
Dicruridae	Dicrurus macrocercus	USNM	292203
Dicruridae	Dicrurus megarhynchus	USNM	615058
Monarchidae	Myiagra hebetor	USNM	615036
Vangidae	Vanga curvirostris	MNHN	2017-254
Dulidae	Dulus dominicus	AMNH	25478
Bombycillidae	Phainopepla nitens	YPM	107690
Bombycillidae	Bombycilla garrulus	YPM	112292
Bombycillidae	Bombycilla cedrorum	YPM	109267
Cinclidae	Cinclus mexicanus	FMNH	288098

Turdidae	<i>Catharus fuscescens</i>	USNM	501951
Turdidae	<i>Turdus merula</i>	NHMUK	S-1975-29-1
Turdidae	<i>Turdus philomelos</i>	MNHN	1997-663
Muscicapidae	<i>Culicicapa ceylonensis</i>	YPM	107307
Muscicapidae	<i>Cichladusa guttata</i>	FMNH	369058
Muscicapidae	<i>Oenanthe oenanthe</i>	AMNH	17960
Sturnidae	<i>Sturnus unicolor</i>	YPM	105055
Sturnidae	<i>Leucopsar rothschildi</i>	USNM	553653
Sturnidae	<i>Buphagus erythrorhynchus</i>	USNM	491371
Mimidae	<i>Toxostoma redivivum</i>	USNM	636895
Sittidae	<i>Sitta europaea</i>	NHMUK	S-1952-2-669
Mimidae	<i>Donacobius atricapilla</i>	UMMZ	227,534
Troglodytidae	<i>Thryothorus ludovicianus</i>	YPM	108237
Paridae	<i>Parus atricapillus</i>	YPM	103511
Hirundinidae	<i>Hirundo rustica</i>	YPM	104483
Reguliidae	<i>Regulus satrapa</i>	NHMUK	S-1998-103-25
Sylviidae	<i>Bernieria zosterops</i>	YPM	103512
Pycnonotidae	<i>Nicator chloris</i>	AMNH	24864
Cisticolidae	<i>Cisticola cantans</i>	FMNH	313190
Sylviidae	<i>Locustella naevia</i>	NHMUK	S-1981-66-1
Sylviidae	<i>Acrocephalus arundinaceus</i>	YPM	101265
Sylviidae	<i>Sylvietta leucophrys</i>	FMNH	346504
Sylviidae	<i>Hylia prasina</i>	AMNH	19071
Sylviidae	<i>Phylloscopus ruficapilla</i>	FMNH	356787
Timaliidae	<i>Garrulax galbanus</i>	CM	S-16131
Timaliidae	<i>Illadopsis cleaveri</i>	NHMUK	S-1911-5-31-357
Timaliidae	<i>Stachyris whiteheadi</i>	FMNH	3877432
Timaliidae	<i>Rhopocichla atriceps</i>	FMNH	355736
Timaliidae	<i>Leiothrix lutea</i>	YPM	103271
Timaliidae	<i>Yuhina brunneiceps</i>	YPM	107381
Sylviidae	<i>Oxylabes madagascariensis</i>	FMNH	384714
Alaudidae	<i>Calandrella rufescens</i>	NHMUK	S-1952-2-601
Dicaeidae	<i>Dicaeum ignipectus</i>	FMNH	392315
Melanocharitidae	<i>Melanocharis versteri</i>	YPM	106461
Passeridae	<i>Passer domesticus</i>	USNM	604859
Motacillidae	<i>Motacilla alba</i>	FMNH	106864
Prunellidae	<i>Prunella modularis</i>	NHMUK	S-1973-25-1
Ploceidae	<i>Ploceus nigricollis</i>	AMNH	17116
Estrildidae	<i>Taeniopygia guttata</i>	YPM	102820
Viduidae	<i>Vidua macroura</i>	FMNH	313258
Fringillidae	<i>Bucanetes githagineus</i>	MNHN	1997-561
Fringillidae	<i>Loxia leucoptera</i>	USNM	622723
Emberizidae	<i>Emberiza cirlus</i>	MNHN	1997-753
Emberizidae	<i>Calcarius lapponicus</i>	NHMUK	S-1958-20-1
Emberizidae	<i>Plectrophenax nivalis</i>	FMNH	428968
Emberizidae	<i>Spizella passerina</i>	NHMUK	S-1955-1-48
Emberizidae	<i>Pipilo chlorurus</i>	AMNH	21692
Parulidae	<i>Dendroica petechia</i>	NHMUK	S-1986-60-66
Thraupidae	<i>Tangara schrankii</i>	CM	S-15320
Emberizidae	<i>Geospiza fortis</i>	USNM	345593

Emberizidae	<i>Geospiza fuliginosa</i>	USNM	345595
Cardinalidae	<i>Cardinalis cardinalis</i>	AMNH	26587
Cardinalidae	<i>Saltator albicollis</i>	AMNH	7249
Icteridae	<i>Psarocolius wagleri</i>	UMMZ	209,355
Icteridae	<i>Quiscalus mexicanus</i>	YPM	107757

Institutional abbreviations: AMNH: American Museum of Natural History, New York, CM: Carnegie Museum, Pittsburgh, FMNH: Field Museum, Chicago, MNHN: Muséum National d'Histoire Naturelle, Paris, NHMUK, Natural History Museum, London, UMMZ: University of Michigan Museum of Zoology, Ann Arbor, USNM: National Museum of Natural History, Smithsonian Institution, YPM: Yale Peabody Museum, New Haven,

Supplemental Data 2: Landmark Definitions

Anatomical Landmarks

Landmark Number	Definition
1	Tip of rostrum, palatal surface, midline
2	Posterior most point of choana at midline
3	Ventral contact between premaxilla and jugal bar (right side)
4	Tip of rostrum, anterodorsal side, midline
5	Median point of craniofacial hinge
6	Anterodorsal limit of the frontal contribution to the orbit-lacrimal contact (right side)
7	Anteroventral contact between pterygoid and palatal surface (right side)
8	Tip of zygomatic process of squamosal (right side)
9	Medial point of contact between parietal and supraoccipital
10	Medial point of dorsal margin of foramen magnum
11	Medial point of dorsal surface occipital condyle
12	Medial point of ventral surface occipital condyle
13	Medial point of contact between basicoccipital and basisphenoid
14	Anterior most point of basisphenoid, just posterior to the pterygoids and palate
15	Posteromedial corner of articular process of quadrate (right side)
16	Anterolateral corner of articular process of quadrate (right side)
17	Posterior point of pterygoid-quadrate articulation (right side)
18	Anterior point of pterygoid-quadrate articulation (right side)
19	Anterior most point of external naris (right side)
20	Posterior most point of ventral (lateral) margin of external naris (right side)
21	Posterior most point of dorsal (medial) margin of external naris (right side)
22	Lateral extreme of frontonasal contact (right side)
23	Ventral contact between premaxilla and jugal bar (left side)
24	Anterodorsal limit of the frontal contribution to the orbit-lacrimal contact (left side)
25	Anteroventral contact between pterygoid and palatal surface (left side)
26	Tip of zygomatic process of squamosal (left side)
27	Posteromedial corner of articular process of quadrate (left side)
28	Anterolateral corner of articular process of quadrate (left side)

29	Posterior point of pterygoid-quadratoarticular articulation (left side)
30	Anterior point of pterygoid-quadratoarticular articulation (left side)
31	Anterior most point of external naris (left side)
32	Posterior most point of ventral (lateral) margin of external naris (left side)
33	Posterior most point of dorsal (medial) margin of external naris (left side)
34	Lateral extreme of frontonasal contact (left side)
35	Lateral extreme of posterior margin of basisphenoid (right side)
36	Lateral extreme of posterior margin of basisphenoid (left side)

Semi-landmark curves:

Curve	Number of sliding semilandmarks	Initial Fixed Landmark	Terminal Fixed Landmark	Definition
1	30	1	2	Midline of the palate
2	20	1	3	Lateral margin of palate
3	10	4	3	Lateral margin of premaxilla
4	30	3	6	Perimeter of jugal bar and the anterior margin of the antorbital fenestra
5	20	6	8	Lateral margin of the orbit
6	10	4	5	Midline of the dorsal side of rostrum
7	10	5	9	Midline of the dorsal side of cranial vault
8	10	9	20	Midline of supraoccipital
9	10	10	11	Lateral margin of foramen magnum
10	10	11	12	Lateral margin of occipital condyle
11	20	9	13	Lateral margin of occipital complex
12	5	13	12	Midline of suboccipital region
13	30	7	3	Posterolateral margin of palate
14	20	13	14	Midline of basisphenoid
15	10	15	16	Posterior margin of articular surface of quadrate
16	10	16	15	Anterior margin of articular surface of quadrate
17	10	17	7	Medial edge of pterygoid
18	10	7	18	Lateral edge of pterygoid
19	10	18	17	Contact between pterygoid and quadrate
20	10	19	20	Ventrolateral margin of naris

21	10	19	21	Dorsomedial margin of naris
22	10	5	22	Craniofacial hinge/frontonasal suture
23	20	14	35	Lateral margin of basisphenoid

Surface semi-landmark patches

Region	Number of Landmarks
Rostrum	102
Palate	72
Pterygoid, ventral surface	20
Quadrato, articular surface	16
Basisphenoid	36
Occipital region	49
Cranial Vault	104
Total:	399